Renewable Energy 225 (2024) 120251

Contents lists available at ScienceDirect

Renewable Energy

journal homepage: www.elsevier.com/locate/renene

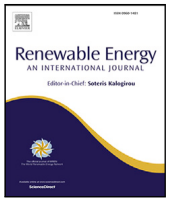

An improved analytical framework for flow prediction inside and downstream of wind farms

Marwa Souaiby, Fernando Porté-Agel *

Wind Engineering and Renewable Energy Laboratory (WiRE), École Polytechnique Fédérale de Lausanne (EPFL), EPFL-ENAC-IIE-WIRE, CH-1015 Lausanne, Switzerland

ARTICLE INFO

Keywords:
Large-eddy simulation
Analytical modelling
Atmospheric boundary layer
Wind farm
Wakes

ABSTRACT

This study evaluates available analytical wake models for flow prediction inside and downstream of wind farms of different sizes and layouts using large-eddy simulation (LES), and introduces an enhanced analytical framework. All the tested analytical wake models, based on the superposition of individual turbine wakes, systematically overestimate the wake recovery both inside and downstream of the wind farms. The results indicate that the overestimation is linked to the assumption of linear or quasilinear wake expansion, which does not hold at large downstream distances. To address this issue, an enhanced analytical framework is proposed based on the extension of a recently developed streamwise scaling model for single wakes that eliminates the need for the linear wake expansion assumption. Since the new framework computes the wake expansion based on the near-wake length and the local turbulence intensity, different methods for their calculation and the superposition of turbulence intensity within wind farms are evaluated against the LES data. The identified best methods are incorporated into the new analytical framework. The proposed framework consistently yields more accurate power estimates and flow predictions inside and downstream of finite-size wind farms with different sizes and configurations.

1. Introduction

The European wind energy sector is projected to experience significant growth from 2023 to 2027, with an estimated installation of 129 GW of new wind farms [1]. This expansion aligns with the European Climate Law, which has been legally enforced by the European Commission to achieve net-zero greenhouse gas emissions by 2050 [2]. As a result, investments in renewable energies, including wind energy, are expected to increase. To ensure the success of new and existing wind energy projects, simple and accurate analytical wake flow models are crucial, as they provide computationally efficient predictions that can be used for optimizing wind farm design and control. Turbine wakes are the primary reason behind the incurred power losses inside a wind farm, especially when the wind direction aligns the turbines in such a way that they are most susceptible to the wake effects of upwind turbines [3–5]. Moreover, the individual turbine wakes merge into one wind farm wake, whose effect can be noticeable far downwind. Due to the clustering of wind farms starting to take place offshore [6], farm-to-farm interactions can lead to additional power losses in wind farms downstream. Within the wind energy community, a large variety of wake modelling techniques is available, ranging from large-eddy simulation (LES) to analytical models. LES is an accurate turbulence-resolving computational fluid dynamics tool that has been validated and widely applied in wind farm flow studies ([7,8], and references therein). However, despite its accuracy, LES is computationally complex and costly compared to analytical models, which offer a more cost-effective, albeit less accurate, alternative for several practical applications such as wind farm layout optimization and real-time control. Therefore, improving the accuracy and robustness of analytical models is considered to be essential to ensure reliable outcomes when optimizing wind farm configuration and control. Moreover, besides their practical value, analytical wake models provide a fundamental understanding of the underlying physics as they are derived from conservation equations governing basic flow properties [9–11].

Engineering wake models based on the superposition of individual wind turbine wakes are widely used to predict the 3D spatial distribution of the flow inside and downwind of finite-size wind farms. One prominent analytical model based on mass conservation was introduced by Jensen [9]. Jensen's model employs a top-hat distribution to represent the wind velocity deficit in the wake of an individual turbine and assumes a constant wake growth rate. To account for wake superposition within a wind farm, the Park model developed by Katic et al. [12] implements the linear superposition of energy deficit. In

* Corresponding author.
E-mail address: fernando.porte-agel@epfl.ch (F. Porté-Agel).

https://doi.org/10.1016/j.renene.2024.120251
Received 5 December 2023; Received in revised form 27 February 2024; Accepted 1 March 2024
Available online 2 March 2024

Nomenclature

Acronyms

ADM-BE	Blade Element Actuator Disk Model
ADM-R	Actuator Disk Model with Rotation
ALM	Actuator Line Model
CNBL	Conventionally Neutral Boundary-Layer
CWBL	Coupled Wake Boundary-Layer Model
LES	Large-eddy simulation
SGS	Subgrid-scale
TurbOPark	Turbulence Optimized Park Model

Key Variables

ΔU_i [m/s]	Wind velocity deficit induced by turbine i in analytical models
ΔU_{max} [m/s]	Maximum wind velocity deficit
δ_{BL} [m]	Boundary-layer height
Γ [K/km]	Free atmosphere stratification level
ω [deg]	Wind direction
σ	Gaussian wake width
θ [K]	Potential temperature
a	Induction factor
A_0 [m^2]	Rotor swept area
A_w [m^2]	Cross-sectional area of a turbine wake
C_p	Power coefficient
C_T	Thrust coefficient
D [m]	Rotor diameter
D_w [m]	Wake diameter
f_c	Coriolis parameter
G [m/s]	Geostrophic wind velocity
I_0	Hub height ambient flow streamwise turbulence intensity
I_U	Streamwise turbulence intensity
I_U^+	Added streamwise turbulence intensity
k^*	Wake growth rate
M [m/s]	Mean wind velocity magnitude from LES
M_∞ [m/s]	Hub height ambient flow mean wind velocity from LES
P [kW]	Power output
U [m/s]	Streamwise wind velocity in analytical models
u_* [m/s]	Friction velocity
U_0 [m/s]	Inflow velocity for a wind turbine inside the farm
U_∞ [m/s]	Undisturbed inflow velocity for the wind farms
U_c [m/s]	Mean convection wind velocity
u_c [m/s]	Relative mean convection wind velocity
x' [m]	Downstream distance from the turbine location
x_0 [m]	Expansion region length
x_{NW} [m]	Near-wake length
z_0 [m]	Surface roughness
z_h [m]	Hub height

an effort to improve the Park model and consider the variability of the wake growth rate within the farm, Stevens et al. [13] coupled it with the one-dimensional top-down model developed by Calaf et al. [14] and introduced the Coupled Wake Boundary-Layer (CWBL) model. The Park model has been further improved by Nygaard et al. [15], who proposed in the Turbulence Optimized Park Model (TurbOPark) an analytical solution for the wake width assumed to expand linearly with the rotor-generated turbulence intensity.

Another common analytical wake model is the Gaussian model, derived by Bastankhah and Porté-Agel [11] by assuming a Gaussian distribution for the wind velocity deficit behind a wind turbine and applying conservation of mass and momentum. Niayifar and Porté-Agel [16] developed an analytical framework implementing the Gaussian model and the principle of linear superposition of wind velocity deficit to superimpose the turbine wakes inside a wind farm. An empirical linear relation, derived from LES results and validated against experimental data, is used in that framework to account for the variability of wake growth rate based on incoming turbulence intensity. More recently, Zong and Porté-Agel [17] introduced another analytical wake modelling framework that implements the Gaussian model to predict individual turbine wakes and a novel wake superposition method that conserves the total momentum deficit in the streamwise direction.

Stieren and Stevens [18] tested the accuracy of some of the above-mentioned analytical models using LES results of flow through a wind farm in a neutrally-stratified boundary layer, and showed that they all tend to over-predict the recovery of the wind farm wake. More recently, Vahidi and Porté-Agel [19] demonstrated that the commonly assumed linear relationship between the turbine wake width and the downstream distance does not hold true for stand-alone wind turbines. Moreover, Vahidi and Porté-Agel [20] found that the normalized maximum wake velocity deficit downwind of an individual turbine, normalized by the rotor diameter, collapsed into a single curve when plotted against the downstream distance, normalized by the near-wake length. Based on these results, they proposed a non-linear relation to compute the normalized maximum wake velocity deficit downstream of a stand-alone wind turbine as a function of the normalized downwind distance. It should be noted that its applicability for predicting wind farm flows remains unexplored.

Turbulence intensity is a key quantity in several analytical models, as it is used to prescribe the wake growth rate [15–17] and to estimate the near-wake length [19,21,22]. For stand-alone wind turbines, several models are available to compute the streamwise variation of the turbulence intensity in the wake. These base models can be divided into two types: simple one-dimensional empirical models to estimate the maximum turbulence intensity at the turbine top tip level [23,24] and three-dimensional models to predict the radial variation of the turbulence intensity in the turbine wake [25,26]. In wind farms, methods for superposing turbulence intensity have received less attention and validation than those for the wind velocity deficit. Recently, Li et al. [27] examined two superposition methods (linear sum and root sum square approaches) for turbulence intensity estimation in a column of wind turbines while applying the three-dimensional model from [26] as a base model. Moreover, they considered normalizing the standard deviation of the wind velocity either by the undisturbed flow velocity at the wind farm inlet or the local wind speed at the inlet of each wind turbine. They found that combining the root sum square method and the normalization by the local wind speed yielded the best results when compared to LES data, although it led to a slight overestimation of the turbulence intensity deep inside the column of wind turbines. Additional analysis is needed to identify the most robust and simple combination of base model and superposition method for the prediction of turbulence intensity inside wind farms with different sizes and configurations.

The main objective of this work is to investigate and enhance the accuracy of analytical wake models by comparing their predictions of the flow inside and downstream of finite wind farms to LES data. The rest of the paper is structured as follows: The implemented LES framework, wind farm cases, and analytical wake models are described in Section 2. In Section 3, several analytical models are evaluated against the LES data, and a new improved analytical framework is introduced and tested. Finally, a summary is provided in Section 4.

2. Numerical frameworks

2.1. LES framework

2.1.1. LES governing equations and modelling

This study implements the in-house WIRE LES code, which solves the spatially filtered incompressible Navier–Stokes equations (Eqs. (1)–(2)). Additionally, the filtered transport equation for potential temperature is solved (Eq. (3)) to account for thermal effects.

$$\frac{\partial \tilde{u}_i}{\partial x_i} = 0 \quad , \tag{1}$$

$$\frac{\partial \tilde{u}_i}{\partial t} + \partial \tilde{u}_j \frac{\partial \tilde{u}_i}{\partial x_j} = -\frac{\partial \tilde{p}^*}{\partial x_i} + \frac{\partial \tilde{\tau}_{ij}^d}{\partial x_j} + \delta_{ij} g \frac{\tilde{\theta} - \langle \tilde{\theta} \rangle}{\theta_0} - \frac{f_i}{\rho} + F_i \quad , \tag{2}$$

$$\frac{\partial \tilde{\theta}}{\partial t} + \tilde{u}_j \frac{\partial \tilde{\theta}}{\partial x_j} = -\frac{\partial \tilde{q}_j}{\partial x_j} \quad . \tag{3}$$

In the equations above, $\tilde{u}_i$ is the filtered wind velocity in the i-direction, $\tilde{\theta}$ is the filtered potential temperature, θ_0 is the reference temperature and the angle brackets denote horizontal averaging. τ_{ij}^d is the deviatoric part of the subgrid-scale (SGS) stress tensor and q_j is the SGS heat flux vector. The SGS turbulent fluxes are modelled using a Lagrangian scale-dependent dynamic model [28,29]. $\tilde{p}^*$ is the modified pressure and δ_{ij} is the Kronecker delta tensor. F_i represents the geostrophic forcing term defined as $F_i = f_c \epsilon_{ij3} \left(\tilde{u}_j - G_j \right)$, where f_c is the Coriolis parameter, ϵ_{ij3} is the Levi-Civita symbol, and G is the geostrophic wind velocity.

The turbine-induced forces, f_i, are parameterized using the blade element actuator disk model (ADM-BE), also known as ADM with rotation (ADM-R). It is implemented to calculate the lift and drag forces as a function of the local simulated flow and the blade characteristics [30]. The ADM-BE is the most suitable method in terms of accuracy and computational cost for this study considering large wind farms, compared to the standard actuator disk model (ADM) and the actuator line model (ALM) [31,32]. The implemented turbines are Vestas V-80 2 MW with a rotor diameter $D = 80$ m and a hub height of $z_h = 70$ m. The power curve already validated by Wu and Porté-Agel [33] is implemented to estimate the power output based on the local wind velocity.

2.1.2. Numerical setup

The WIRE LES code is implemented to study the interactions between wind farms with different sizes and configurations, and the conventionally neutral boundary layer (CNBL). The code is a modified version of the one introduced by Albertson and Parlange [34], Porté-Agel et al. [28], Stoll and Porté-Agel [29], and Abkar and Porté-Agel [35]. The computational domain with dimensions L_x, L_y, and L_z is discretized into N_x, N_y and N_z evenly spaced grid points in the streamwise, spanwise and vertical directions, respectively. The grid planes are staggered in the vertical direction, with the first vertical velocity plane located at $\Delta_z = L_z / \left(N_z - 1 \right)$, and the lowest plane of the other variables such as pressure, horizontal wind velocity components, and potential temperature located at $\Delta_z/2$ from the surface. A second-order Adams–Bashforth explicit scheme is executed for time advancement, and a hybrid pseudo-spectral finite-difference scheme is applied for spatial discretization. The spatial derivatives are evaluated using a pseudo-spectral method in the streamwise and spanwise direction and a second-order finite-difference approximation in the vertical direction. Full dealiasing of the nonlinear terms is accomplished through explicit filtering. The lateral boundary conditions are set to be periodic. A flux-free condition is assigned to the upper boundary with a Rayleigh damping layer of 300 m to reduce any gravity wave reflection [36,37]. The temperature gradient is fixed at $\Gamma = 1$ K/km at the top boundary. At the bottom surface, the local instantaneous shear stress is calculated as a function of the local filtered horizontal wind velocity $\tilde{u}_r$ at the lowest vertical grid point $(\Delta_z/2)$ using Monin–Obukhov similarity theory [38]. Even though this theory was originally formulated for averaged quantities, it is a common approach in LES of atmospheric flows [39,40] to calculate the instantaneous filtered surface momentum flux under neutral conditions as follows:

$$\tau_{i3}|_w = -u_*^2 \frac{\tilde{u}_i}{\tilde{u}_r} = -\left(\frac{\tilde{u}_r}{ln\left(z/z_0\right)} \right)^2 \frac{\tilde{u}_i}{\tilde{u}_r} \quad , \tag{4}$$

where $\tau_{i3}|_w$ is the instantaneous wall stress, u_* is the friction velocity, z_0 is the surface roughness, and $\kappa = 0.4$ represents the von Kármán constant. Given that we are simulating a CNBL, the surface heat flux is set to be zero.

2.2. Suite of simulations

A suite of LES simulations is performed for the no-farm, finite-size wind farm and infinite wind farm cases. The no-farm case acts as a precursor simulation generating the inflow to the wind farms. The infinite wind farm cases have wind turbines placed over the whole domain and, owing to the periodic boundary conditions in both horizontal directions, they represent the infinite regime of the modelled wind farms.

All cases consider a CNBL with a weak free atmosphere stratification level fixed at $\Gamma = 1$ K/km. The flow is driven by a geostrophic wind $G = 10$ m/s and the Coriolis parameter used is $f_c = 1.195 \times 10^{-4}$ rad/s. In the no-farm and infinite wind farm cases, the initial temperature profile starting from the reference temperature $\theta_0 = 293$ K is kept constant vertically up to 100 m and then follows the set lapse rate Γ. The surface roughness is set to $z_0 = 0.05$ m. The cases are initialized with a constant streamwise wind velocity of 10 m/s. Additionally, to stimulate the development of turbulence inside the ABL, small random perturbations are added to the initial wind velocity and temperature fields at the lowest 100 m of the domain. All the simulations are run for a long enough duration to guarantee that quasi-stationary conditions are achieved.

2.2.1. No-farm case

Fig. 1 shows the vertical profiles of the time- and horizontally-averaged ambient flow characteristics of the no-farm case, where at hub height the mean wind velocity (M_∞) is 7.75 m/s and the ambient flow streamwise turbulence intensity (I_0) is 10%. Two different methods are used to calculate the boundary layer height, δ_{BL}. In the first method, δ_{BL} is defined as the height at which the total momentum flux reaches 5% of its surface value. For this definition, δ_{BL} of the no-farm case reaches 800 m as shown in Fig. 1(a). In the second method, δ_{BL} is determined as the lowest elevation at which the mean wind velocity magnitude (M) equals the geostrophic value (G). Applying this method, δ_{BL} is found to be 430 m, as also shown in Fig. 1(a).

2.2.2. Finite wind farm cases

A suite of 16 LES simulations is conducted for a combination of four different wind farm sizes, two different wind farm densities, and two possible layouts: aligned and staggered. To ensure analysing the operation of wind farms in a fully developed ABL, the no-farm case acting as a precursor simulation to generate the needed inflow is run first long enough to guarantee stationary flow conditions. The flow generated in the no-farm simulation is then fed at the inlet of the finite-size wind farms, and a buffer zone is used to seamlessly adjust the flow from the far-wake wind farm flow to the inflow [33]. The wind farms are placed 2 km from the inlet, and a long enough domain is considered to be able to investigate the wind farm wake up to a downstream distance of 10 km as illustrated in Fig. 2. The wind farm is infinite in the spanwise direction due to the periodic lateral boundary condition. A wind direction control, comparable to the one previously implemented in the literature [41–43], is applied over the wind velocity field to ensure that the mean wind flow velocity at the wind turbines is always perpendicular to the rotor. Specifically, a source term is introduced to the momentum conservation equations to

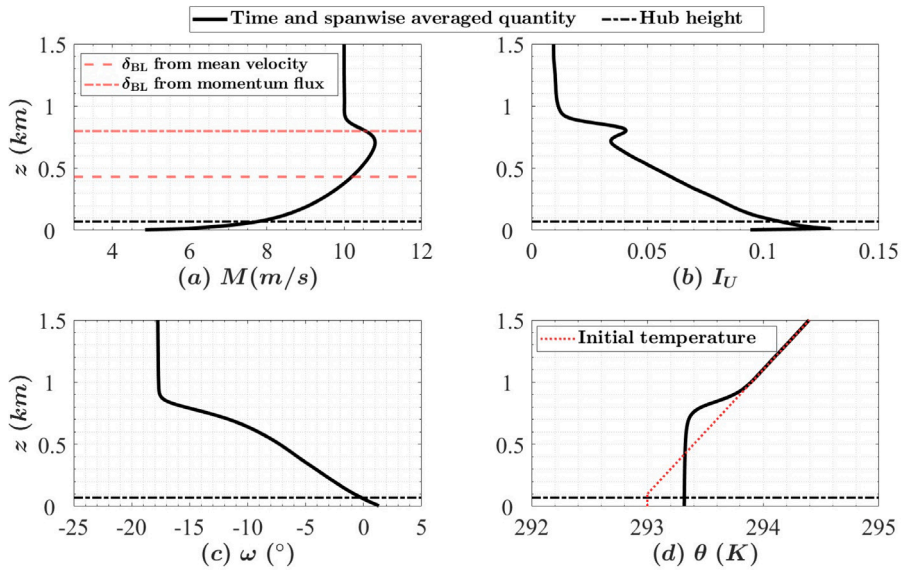

Fig. 1. Vertical profiles of the time- and horizontally-averaged ABL flow characteristics in the precursor no-farm case: (a) wind velocity magnitude, M (m/s); (b) streamwise turbulence intensity, I_U; (c) wind direction, ω (°); (d) potential temperature, θ (K).

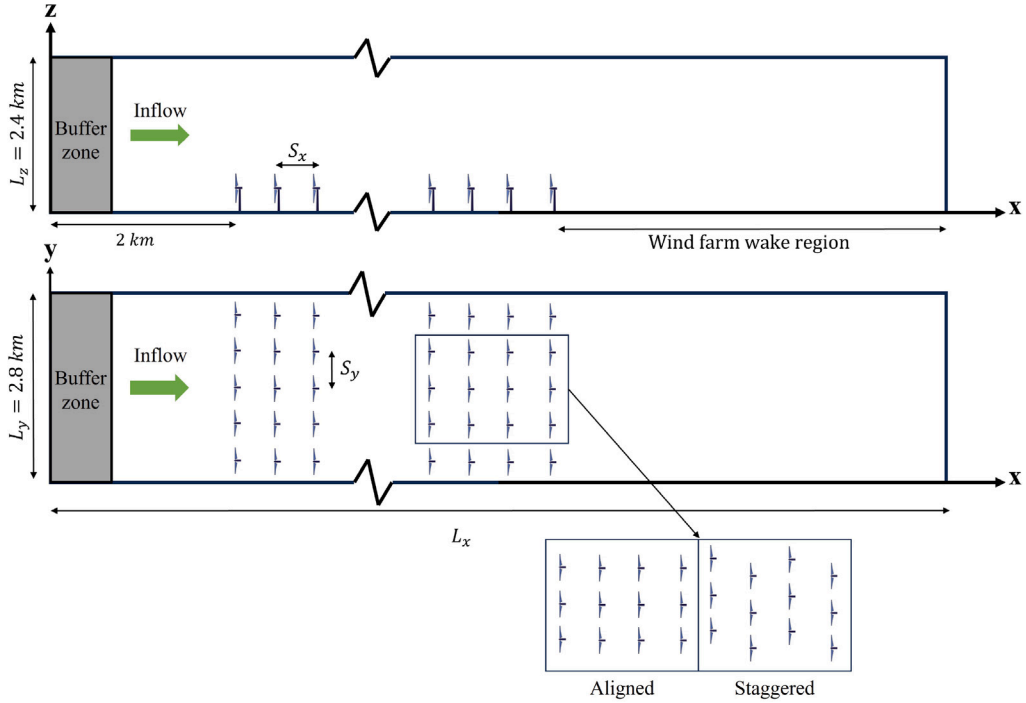

Fig. 2. Computational domain and layout of the simulated finite-size wind farms. Note: This figure is not drawn to scale.

gradually adjust the geostrophic wind direction. The main parameters of the different simulated cases are summarized in Table 1, where the streamwise and spanwise turbine spacing normalized by the rotor diameter are represented by S_x and S_y, respectively. The implemented grid size for the simulations covers the turbine rotor by a minimum of eight points vertically and seven points laterally, satisfying the requirements set in previous validation studies. Specifically, Wu and Porté-Agel [30,44] demonstrated that the WIRE-LES code yields wind velocity and turbulence intensity fields with low grid dependence as long as the turbine rotor is covered by at least seven mesh points in the vertical direction and five in the spanwise direction. All the wind farm simulations are run for 4 h and the needed data is gathered and averaged over the last 3 h when quasi-steady flow conditions are reached.

2.2.3. *Infinite wind farm cases*

To evaluate the flow characteristics within large wind farms, it is useful to establish a reference case that represents the infinite wind farm regime. In this study, four infinite wind farms are modelled using the periodic boundary condition in both horizontal directions and, unlike the finite-size wind farm cases, not including the aforementioned buffer and inflow regions. The domain comprises 12 and 14 turbine rows, corresponding to a turbine spacing of 7D and 5D, respectively. The flow statistics are averaged over the last 6 h of the simulations, after a sufficiently long running time to ensure that the flow reaches the fully-developed infinite regime.

Table 1
Key parameters of the suite of LES finite-size wind farm simulations.

Case	*rows* × *columns*	$S_x \times S_y$	Layout	$L_x \times L_y \times L_z$ (km^3)	$N_x \times N_y \times N_z$
Size 1					
S1-A-7	9 × 7	$7D \times 7D$	Aligned	$22.4 \times 2.8 \times 2.4$	$960 \times 256 \times 256$
S1-S-7	9 × 7	$7D \times 7D$	Staggered	$22.4 \times 2.8 \times 2.4$	$960 \times 256 \times 256$
S1-A-5	9 × 5	$5D \times 5D$	Aligned	$22.4 \times 2.8 \times 2.4$	$960 \times 256 \times 256$
S1-S-5	9 × 5	$5D \times 5D$	Staggered	$22.4 \times 2.8 \times 2.4$	$960 \times 256 \times 256$
Size 2					
S2-A-7	18 × 7	$7D \times 7D$	Aligned	$28 \times 2.8 \times 2.4$	$1200 \times 256 \times 256$
S2-S-7	18 × 7	$7D \times 7D$	Staggered	$28 \times 2.8 \times 2.4$	$1200 \times 256 \times 256$
S2-A-5	18 × 5	$5D \times 5D$	Aligned	$22.4 \times 2.8 \times 2.4$	$960 \times 256 \times 256$
S2-S-5	18 × 5	$5D \times 5D$	Staggered	$22.4 \times 2.8 \times 2.4$	$960 \times 256 \times 256$
Size 3					
S3-A-7	27 × 7	$7D \times 7D$	Aligned	$33.6 \times 2.8 \times 2.4$	$1440 \times 256 \times 256$
S3-S-7	27 × 7	$7D \times 7D$	Staggered	$33.6 \times 2.8 \times 2.4$	$1440 \times 256 \times 256$
S3-A-5	27 × 5	$5D \times 5D$	Aligned	$28 \times 2.8 \times 2.4$	$1200 \times 256 \times 256$
S3-S-5	27 × 5	$5D \times 5D$	Staggered	$28 \times 2.8 \times 2.4$	$1200 \times 256 \times 256$
Size 4					
S4-A-7	36 × 7	$7D \times 7D$	Aligned	$39.2 \times 2.8 \times 2.4$	$1680 \times 256 \times 256$
S4-S-7	36 × 7	$7D \times 7D$	Staggered	$39.2 \times 2.8 \times 2.4$	$1680 \times 256 \times 256$
S4-A-5	36 × 5	$5D \times 5D$	Aligned	$33.6 \times 2.8 \times 2.4$	$1440 \times 256 \times 256$
S4-S-5	36 × 5	$5D \times 5D$	Staggered	$33.6 \times 2.8 \times 2.4$	$1440 \times 256 \times 256$

2.3. Analytical wake models

In this section, we summarize the implemented analytical wake models used to predict the wind speed variation inside and downstream of the wind farms.

2.3.1. Park model

The Park model implements the top-hat model of Jensen [9] for the prediction of the wake velocity deficit of each individual wind turbine. That model, which assumes a top-hat shape of the wake velocity deficit and is derived based on mass conservation, can be written as follows:

$$\Delta U_i(x') = U_{\infty hub}\left[\frac{D^2}{D_w(x')^2}\left(1-\sqrt{1-C_T}\right)\right] \quad , \tag{5}$$

where ΔU_i is the velocity deficit induced by a wind turbine (i), and defined in this model with respect to the base-flow velocity of the no-farm case (U_∞), which has a value of $U_{\infty hub}$ at hub height. x' is the downstream distance from the turbine with a rotor diameter D and a thrust coefficient C_T. In this model, the wake diameter D_w is assumed to grow linearly with a constant growth rate k^*, i.e.:

$$D_w(x') = 2k^*x' + D \quad , \tag{6}$$

In this study, k^* is set equal to $k^* = \frac{\kappa}{ln(z_h/z_0)}$ as suggested in the literature [45].

In the Park model, the turbine wake interactions inside a wind farm are modelled using the linear superposition of energy deficits introduced by Katic et al. [12]:

$$U(x,y,z) = U_\infty - \sqrt{\sum_i \left(\Delta U_i\right)^2} \quad , \tag{7}$$

where $U(x,y,z)$ is the flow velocity at a point (x,y,z) in the domain.

2.3.2. Turbulence optimized park model

Another widely used analytical wake model is the TurbOPark model, which was introduced by Nygaard et al. [15] as an extension of the Park model. This method uses also the aforementioned Jensen model (Eq. (5)) and linear superposition of energy deficits (Eq. (7)). Unlike the original Park model, the turbine wake diameter D_w is computed as a function of the local turbulence intensity in the wake as follows:

$$D_w(x') = D + \frac{AI_0D}{\beta}\left[\sqrt{(\alpha+\beta x'/D)^2+1} - \sqrt{1+\alpha^2} - ln\left[\frac{\left(\sqrt{(\alpha+\beta x'/D)^2+1}+1\right)\alpha}{\left(\sqrt{1+\alpha^2}+1\right)(\alpha+\beta x'/D)}\right]\right] \quad , \tag{8}$$

where I_0 is the ambient turbulence intensity, $\alpha = 1.5I_0$, $\beta = 0.8I_0/\sqrt{C_T}$, and the calibration parameter $A = 0.6$ [15]. The added turbulence is computed using Frandsen's empirical model [24] described later in Section 3.3.1.

2.3.3. Niayifar and Porté-Agel model

The analytical framework presented by Niayifar and Porté-Agel [16] uses the Gaussian model of Bastankhah and Porté-Agel [11] as a base model to predict the velocity deficit of each individual wind turbine. That model, which assumes a two-dimensional Gaussian shape for the velocity deficit and is derived based on the conservation of mass and momentum, can be written as follows:

$$\Delta U_i(x',y',z') = U_0\left(1-\sqrt{1-\frac{C_T D^2}{8\sigma^2}}\right)exp\left(-\frac{z'^2+y'^2}{2\sigma^2}\right) \quad , \tag{9}$$

where ΔU_i is defined here with respect to the flow velocity inside the wind farm at the position of turbine (i), but not including it. U_0 is the rotor-averaged value of that flow velocity. The three directional coordinates with respect to the centre of turbine (i) are x', y', and z'. The wake width (σ) is assumed to grow linearly and computed as follows Bastankhah and Porté-Agel [22]: $\frac{\sigma}{D} = k^*\frac{(x'-x_{NW})}{D} + \sqrt{\frac{1}{8}}$, where x_{NW} is the near-wake length calculated using the model from [22], and k^* is the wake growth rate computed as a function of the streamwise turbulence intensity using the following empirical linear relation: $k^* = 0.38I_U + 0.004$, which is valid for $C_T = 0.8$ and $0.065 < I_U < 0.15$ [16]. I_U is calculated as a function of the ambient turbulence intensity I_0 and the added streamwise turbulence intensity I_U^+ as such: $I_U = \sqrt{I_0^2 + I_U^{+2}}$. The added turbulence intensity (I_U^+) is found using the empirical relation developed by Crespo and Hernández [23], and only the maximum added turbulence from the closest upwind turbine is considered, as described later in Section 3.3.1. The turbine wake superposition model implemented is the linear superposition of wind velocity deficits as developed by Niayifar and Porté-Agel [16]:

$$U(x,y,z) = U_\infty - \sum_i \Delta U_i \quad . \tag{10}$$

2.3.4. Zong and Porté-Agel model

Zong and Porté-Agel [17] developed a wake superposition model that guarantees the conservation of the total momentum deficit in the streamwise direction. The individual wind turbine wakes are calculated using the Gaussian model of Bastankhah and Porté-Agel [11] (Eq. (9)). The wake width is calculated using the quasi-linear function of [46]. It is simplified here since no yaw angle is considered: $\sigma/D = 0.35 + k^*ln\left[1+exp\left(\frac{x-x_{NW}}{D}\right)\right]$, where x_{NW} and k^* are computed as detailed in the previous model description. The wake superposition is calculated using the following equations:

$$U(x,y,z) = U_\infty - \sum_i \frac{u_c^i(x)}{U_c(x)}\Delta U_i \quad , \tag{11}$$

$$U_c(x) = \frac{\iint \left(U_\infty - U(x,y,z)\right).U(x,y,z)dydz}{\iint \left(U_\infty - U(x,y,z)\right)dydz} \quad , \tag{12}$$

where u_c^i is the relative mean convection velocity of the wake of each upstream turbine i, while U_c is the mean convection flow velocity for the combined wake of all upstream turbines. U_c is obtained

through iterations between Eqs. (11) and (12) and initialized to be the maximum value of u_c^i. Eq. (11) models the total velocity deficit as a weighted sum of the individual wake velocity deficits ΔU_i, where the weights are the ratio of u_c^i to U_c. When merging two wakes with equivalent velocity deficit levels, the one with a higher convection velocity bears a greater momentum deficit, and should consequently be assigned a higher weight. In the special case of dealing with small wake velocity deficits (e.g., if turbine spacing is large), the weight may be approximated as 1, which then transforms Eq. (11) into Eq. (10) of the linear superposition of wind velocity deficits.

3. Results

3.1. Wind farm size and configuration effects

In previous studies, the wind flow properties inside and above wind farms have been extensively investigated ([8], and references therein), yet the effect of the wind farm size and configuration on the wind farm wake region has received less attention. In this section, we use the LES results to investigate the flow characteristics in the wind farm exit and wake regions for the different sizes and configurations considered in this study.

Fig. 3 presents the time-averaged hub height wind velocity distribution in the wake of the simulated wind farms along with the horizontally-averaged hub height wind velocity level reached by the respective infinite cases. Specifically, Fig. 3(a) shows streamwise profiles of the spanwise-averaged mean wind velocity as well as the row-averaged wind speed over the last wind farm rows, while Fig. 3(b) depicts the evolution of the mean hub height wind speed at the column centre. All the wind velocity profiles are normalized by the hub height wind velocity from the no-farm case. From Fig. 3(b), we can observe that the wind farm size has a relatively small effect on the maximum wind velocity deficit, since the column-centred wind velocity plots for all considered farm sizes overlap. On the contrary, the spanwise averaged profiles exhibit significant variation across different wind farm sizes. This is demonstrated by a decrease in the mean wind speed with increasing wind farm size at any considered streamwise position relative to the wind farm exit. These changes become smaller with increasing wind farm size. At the downstream end of the wind farm, the row-averaged mean wind speed drops by around 5% from the 9-row cases to the 18-row cases. Considering that these sizes are within the typical range of sizes of existing and planned wind farms, these results highlight the importance of accounting for size effects on the prediction of wind speed deep inside the wind farm as well as the wind farm wake. In larger wind farm cases of 27 and 36 rows, the decrease in the exit wind velocity is around 1%, which is less significant. Compared to the horizontally averaged wind velocity obtained from the infinite wind farm cases, the largest wind farms approach this infinite asymptotic limit at the end of the farm albeit not reaching it.

It is worth mentioning that the hub height spanwise-averaged mean wind speed deficit in the wind farm wakes remains noticeable at a downwind distance of 10 km. It still shows some dependence on wind farm size and configuration, and its value ranges from 2% to 5%. This observation aligns with the findings of Christiansen and Hasager [47] and Wu and Porté-Agel [43]. Similar results were also discussed by Stieren and Stevens [18], who investigated the interaction between two wind farms. The wind farm positioned 10 km downstream experienced an 11% reduction in power at their first row compared to the upstream wind farm.

Figs. 4 and 5 show the contour plots of the time-averaged wind speed and streamwise turbulence intensity, respectively, on a horizontal plane at hub height showing the simulated wind farm exit and wind farm wake regions. In the shortest considered farms (9 and 18 rows) with the lowest density ($7D$ cases) and aligned configuration, which are commonly encountered offshore for certain wind directions [48–51] the flow is highly heterogeneous in the spanwise direction within the entire wind farm. This is due to the fact that the wind turbine wake effects remain constrained to localized regions around the turbine columns, which are separated by channels of high-speed wind flow. According to Wu and Porté-Agel [43], the high-speed channels in aligned cases were identified as a significant factor contributing to the increased flow heterogeneity observed in these configurations. In those cases, the spanwise heterogeneity of the mean wind speed is evident in the wind farm exit region and in the farm wake up to a distance of about 5 km. At longer downstream distances, the lateral expansion and interaction of the wind turbine wakes lead to a more homogeneous wind farm wake flow.

For the wind farm cases with staggered configuration, the lateral flow heterogeneity at the wind farm exit becomes smaller compared to their aligned counterparts and extends for shorter distances downstream, as illustrated by both the wind velocity and turbulence intensity contour plots. This is due to the larger spanwise wake interactions associated with the relatively smaller lateral distance between adjacent wind turbine wakes as a result of staggering. Likewise, for a given wind farm layout, increasing the wind farm size leads to smaller flow heterogeneity at the wind farm exit and wake regions, owing to the increased spanwise expansion of the cumulated wakes. It is noteworthy that greater maximum turbulence intensity levels are found in aligned wind farms when compared to their staggered counterparts. This finding is consistent with the results of Markfort et al. [52], Wu and Porté-Agel [53,54]. Similar to the wind speed deficit, the turbulence intensity also increases as the size and/or density of the wind farm increases.

Fig. 6 presents the normalized power output averaged over each row. It is shown that, for any given wind farm density and configuration, the streamwise evolution of the power output is not affected by wind farm size. In all the considered cases, the power output of the last rows remains greater by 5% on average than the power output level of the infinite wind farm cases. This observation is similar to the results presented by Wu and Porté-Agel [43], where the power output inside the wind farm simulated in a CNBL with a weak stratification level remained steady and larger than the infinite wind farm power level. The power output exceeding the infinite wind farm level is consistent with the fact that the spanwise averaged wind speed does not reach the infinite wind farm limit, as previously discussed. These results indicate that the atmospheric boundary layer flow is not yet fully developed and does not reach the infinite wind farm regime, even for the largest farms considered in this study. Wind farm density and configuration are found to have an important effect on the distribution of power output in the simulated wind farms. The power output stabilizes faster in aligned wind farms compared to the more gradual decrease observed in staggered cases. In the aligned wind farm cases, a sharp decrease in power output is observed in the second row, followed by a slight improvement in subsequent rows. This trend is consistent with the findings of Wu and Porté-Agel [33], who attribute the power increase at the third row to the enhanced turbulence level in the wake of the first row, leading to a relatively faster wake recovery after the second row. In the staggered configuration, where the turbine wakes have longer distances to recover before they interact with the closest downstream wind turbine, this behaviour is not observed. The power output gradually decreases within the staggered wind farm, as similarly reported in previous studies showing the power variation inside the Horns Rev wind farm for different wind direction [3,55]. Comparing the two considered wind farm densities, the stabilized power output levels in the low-density wind farms ($7D$ cases) are about 10% higher than the level reached in the high-density wind farms ($5D$ cases) for all considered wind farm configurations and sizes. This can be explained by the fact that in wind farms with higher density of turbines ($5D$ cases) the turbine wakes have a shorter distance to recover before encountering a downstream turbine, thus leading to larger wake-induced power losses.

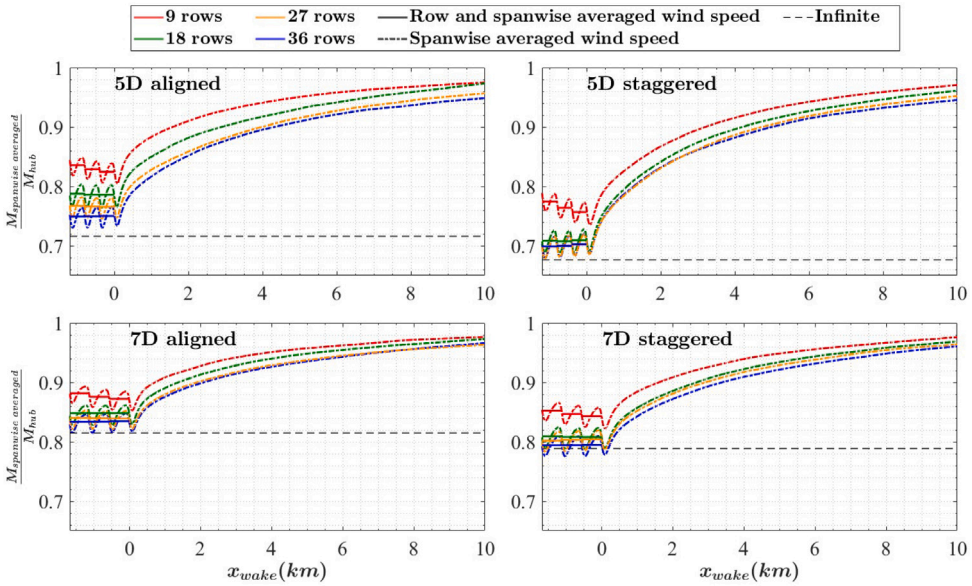

(a) Normalized spanwise-averaged wind velocity magnitude.

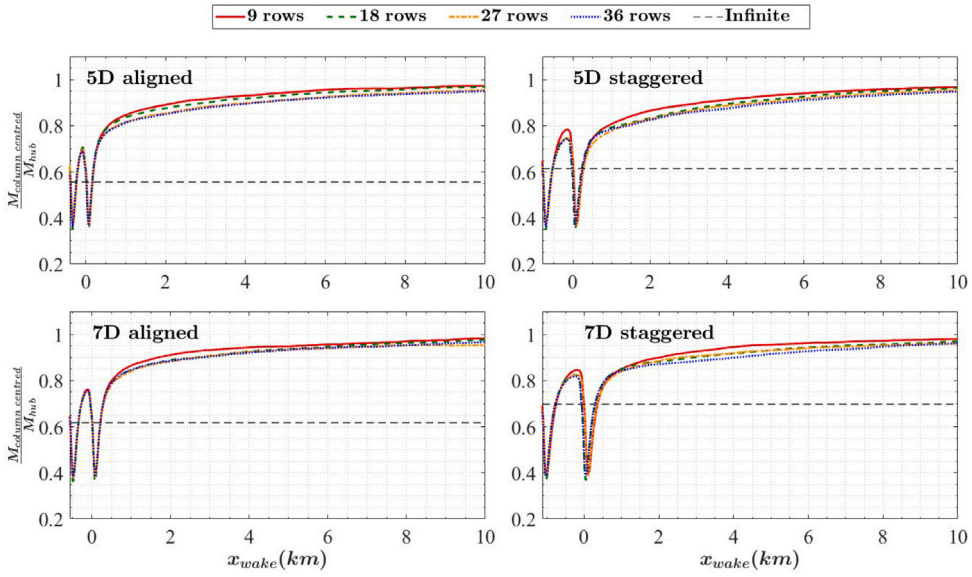

(b) Normalized wind velocity magnitude taken at the center of a wind farm column.

Fig. 3. Normalized wind velocity magnitude variation in the streamwise direction for all considered LES cases.

3.2. Analytical wake models assessment

The previously described analytical wake models are used here to predict the wind velocity inside and downstream of all the wind farms under consideration. Figs. 7 and 8 show the streamwise profiles of the time- and rotor-averaged wind speed at hub height as simulated by LES and predicted by the considered analytical wake models. From these figures, it is clear that all the implemented models tend to overestimate the wake recovery inside and downstream of the wind farms, which is consistent with the results of Stieren and Stevens [18]. Overall, for all the wind farm cases, the Park model gives the largest overestimation of the wind speed in the wind farm wakes for downstream distances larger than about 1 km. This could be related to the fact that the models assume a constant wake growth rate throughout the wind farm, regardless of the variation of turbulence intensity inside the farm.

Fig. 7 shows the simulated and modelled wind velocity fields inside and downstream of the 36-row wind farm, in order to evaluate the capacity of the tested analytical models to capture the effects of wind farm configuration and density. In the staggered cases, regardless of wind farm density, the models of Niayifar and Porté-Agel [16] and Zong and Porté-Agel [17] show the best performance, although still overestimating the mean wind speed in the farm wake. It is important to note that the flow in the near-wake region is not predicted by both Niayifar and Porté-Agel [16] and Zong and Porté-Agel [17], since they are based on the Gaussian model, which is strictly only valid in the far-wake region. Also in the staggered configuration, both the Park and TurbOPark models yield the largest wind speed overestimation. This over-prediction can be attributed to the constant wake growth rate throughout the wind farm in the Park model, and to the method described in Section 2.3 for calculating the wake width in the TurbOPark model. This model takes into account the added turbulence

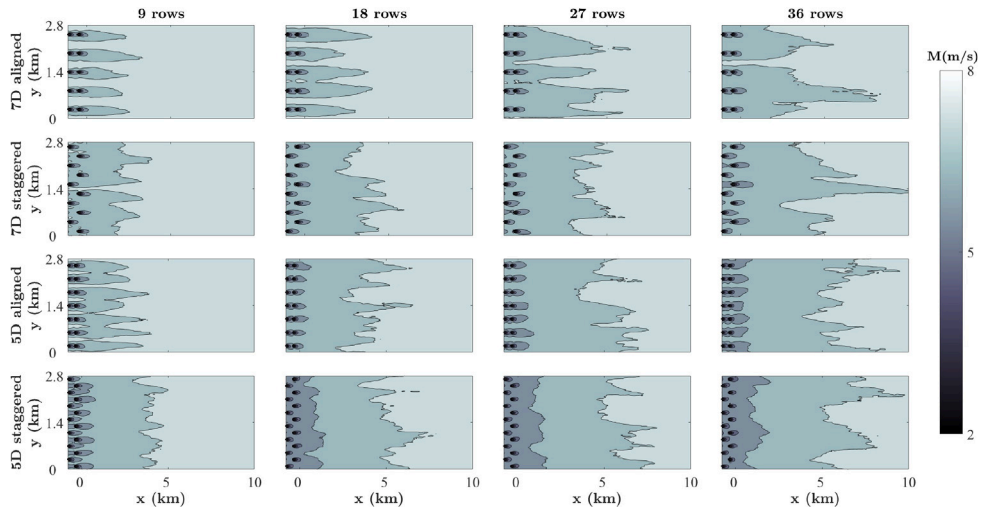

Fig. 4. Contours of the time-averaged mean wind velocity magnitude of the wind farm exit and wake regions at a horizontal plane at hub height for all the considered cases.

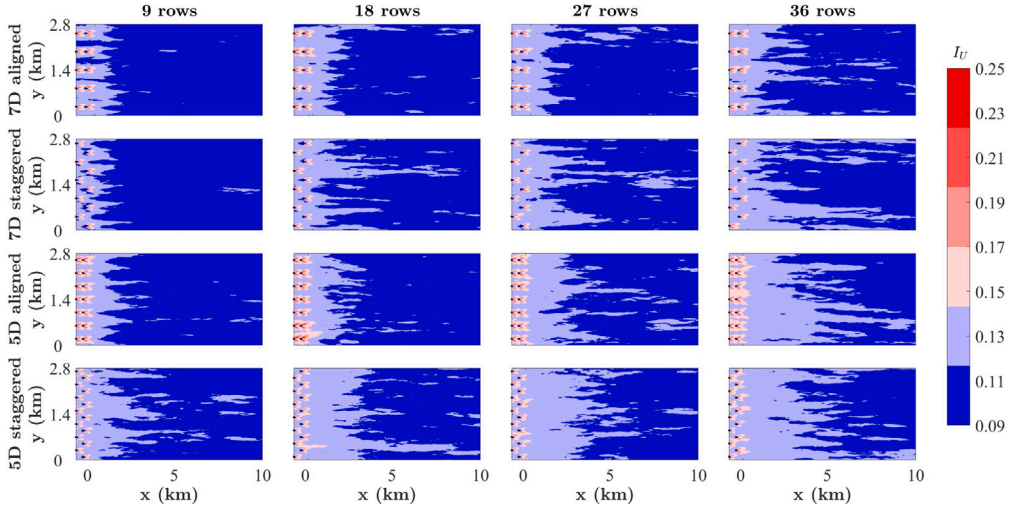

Fig. 5. Contours of the streamwise turbulence intensity at the wind farm exit and wake regions on a horizontal plane at hub height for all the considered cases.

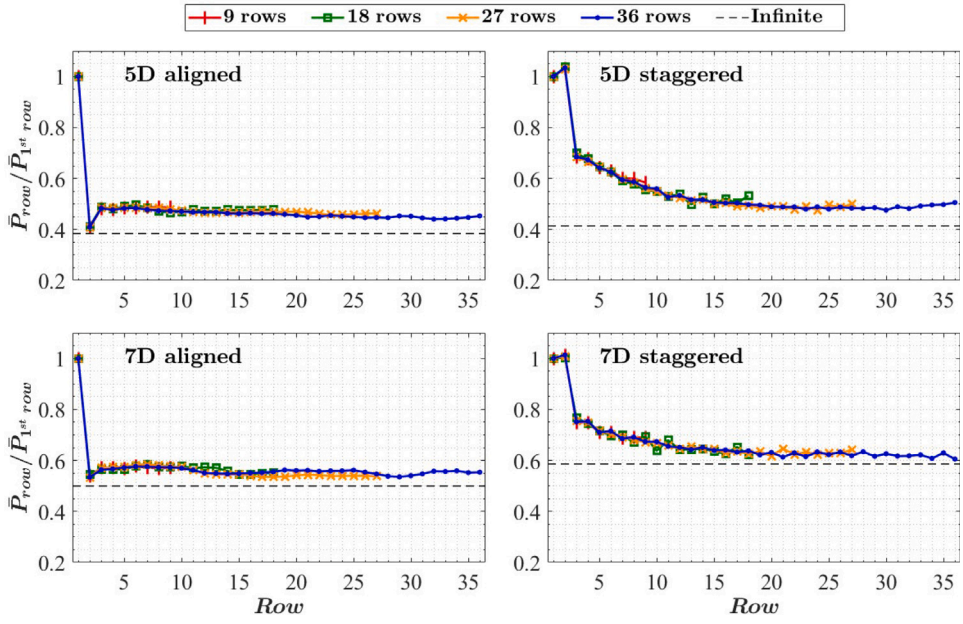

Fig. 6. Power output of different turbine rows inside the wind farms normalized by the power output of the first row.

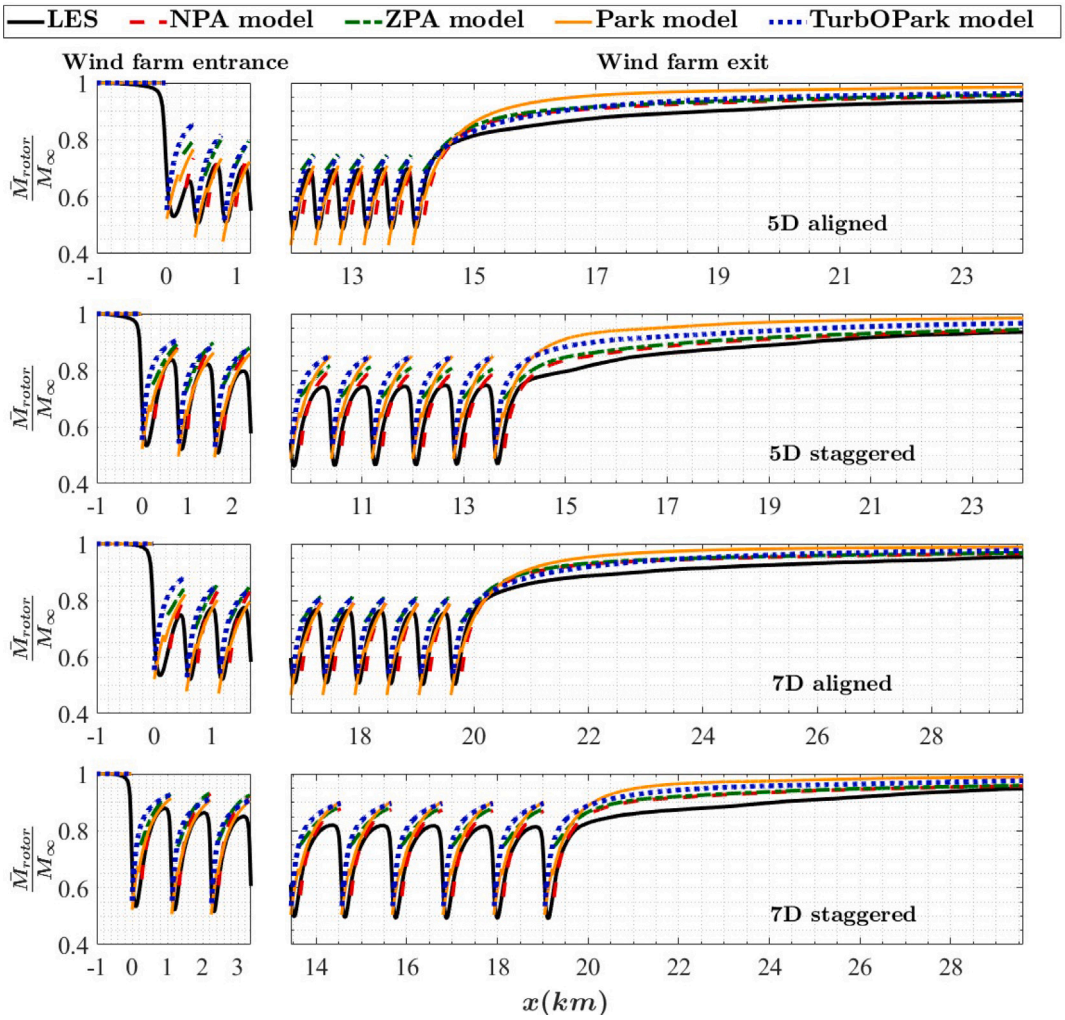

Fig. 7. Rotor-averaged wind speed variation in the entrance, exit and wake regions of the 36-row wind farms of different configurations, as simulated by LES and predicted by all the considered analytical wake models: NPA model [16], ZPA model [17], Park model [12] and TurbOPark model [15].

from the same turbine being modelled, leading to an enhanced level of turbulence intensity, hence a faster wake recovery. In the aligned configuration, the TurbOPark, Niayifar and Porté-Agel [16] and Zong and Porté-Agel [17] models show the best performance albeit their wind speed over-prediction. The TurbOPark model yields the fastest wake recovery behind the first row of wind turbines. This unrealistic overestimation of the wake expansion points to a limitation of the distinct method used by TurbOPark to compute the wake diameter based on the total turbulence in the wake flow (Eq. (8)), instead of only that in the base-flow. This is consistent with the fact that the overestimation in wake recovery is less important in the staggered cases, where the effective streamwise inter-turbine distance is larger, thus allowing the added turbulence levels and the associated wake expansion rate to decay to smaller values before encountering a downstream turbine. The wind speed overprediction in the wake of the first turbine row leads to an overestimation of the power output at the second row by that model, as shown later in Fig. 9. It is worth noting that all the considered analytical wake models are unable to predict the wind speed reduction characteristic of the induction region immediately upstream of the wind turbines. This explains the discrepancies displayed by the models in that region. Yet, this does not affect the power prediction by the models, as they compute the turbine power extraction based on the wind speed of the base flow (i.e., the flow unaffected by the turbine under consideration).

In order to evaluate the ability of the tested analytical wake models to capture the effect of wind farms size, Fig. 8 shows the simulated and modelled wind velocity fields inside and downstream of the $7D$ staggered cases for the four considered wind farm sizes. It is shown that the wind speed overestimation introduced by the models of Niayifar and Porté-Agel [16] and Zong and Porté-Agel [17] remain at a similar level for all the wind farm sizes. On the other hand, the overestimation of the wind speed by the Park and TurbOPark models increases with increasing wind farm size. Therefore, these models are unable to capture the decrease of spanwise-averaged wind speed at any given downstream distance associated with the increase in wind farm size.

The normalized power output over the rows of the wind farm, as simulated by LES and predicted by all models under consideration, are presented in Fig. 9. It is important to note that the observations on the power output are consistent with the rotor-averaged wind velocity estimation within the wind farm as the turbine power output prediction is calculated based on the estimated rotor-averaged wind speed. It is worth noting that a constant C_p of 0.44, derived from the characteristic curves presented by Wu and Porté-Agel [33], is used in all the considered analytical models. The comparison between the power output from LES and the tested analytical models in Fig. 9 depicts that, in the aligned cases, the model of Zong and Porté-Agel [17] gives the most accurate power estimation. The model of Niayifar and Porté-Agel [16] gives a comparable power prediction, yet it delivers an underestimation notably near the end of the high density wind farm ($5D$ case). The discrepancy in power estimates is consistent with the model underestimating the wind speed near the exit of the aligned wind farms. This outcome is consistent with the findings of Zong and Porté-Agel [17]

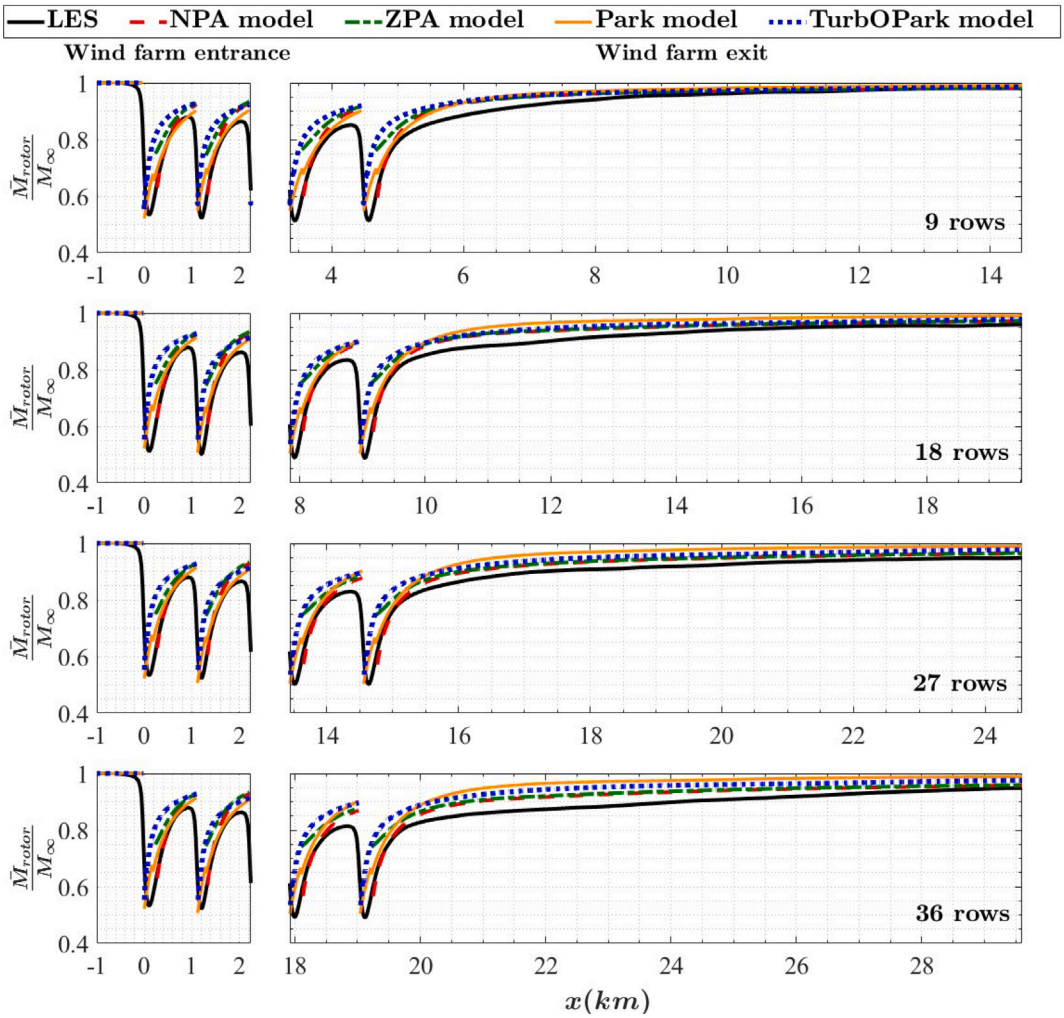

Fig. 8. Rotor-averaged wind speed variation in the entrance, exit and wake regions of the $7D$ staggered wind farms of different sizes, as simulated by LES and predicted by all the considered analytical wake models: NPA model [16], ZPA model [17], Park model [12] and TurbOPark model [15].

who showed that the two models are very similar when the streamwise distance between the turbines is sufficiently large ($x > 13D$). In fact, the power predictions of both models in the $7D$ staggered wind farm with the largest streamwise distance between the turbines ($x = 14D$) are very similar, as opposed to the remaining cases where the difference starts to gradually increase going from a streamwise distance of $x = 10D$, in the $5D$ staggered wind farm, to a distance of $x = 5D$, in the $5D$ aligned case. Additionally, Zong and Porté-Agel [17] accurately predicts the sharp drop behind the first row and then the slight increase at the third row in the aligned cases. In contrast, the observed sharp reduction in power behind the first row is not accurately captured by TurbOPark as discussed before with the observed overestimation of the wake growth rate in Fig. 7 at the wind farm entrance. After the fourth row, however, TurbOPark provides a good power prediction in the aligned cases. As for the Park model, it predicts well the drop in power at the second row, but fails to reproduce the slight recovery at the third row, thus leading to an overall underestimation of the power throughout the rest of the aligned wind farm. The power underestimation introduced by the Park model is consistent with the model's tendency to underestimate the wind speed within aligned wind farms.

Let us now compare the power performance of the various analytical wake models to the LES data in the staggered cases, as shown in the right panels of Fig. 9. In this configuration, the simulated power shows a more gradual decrease with downstream distance, which is consistent with previous studies [43,56]. This relates to the effective downstream distance between adjacent wind turbines, which is double in staggered wind farms compared to aligned ones. This results in longer distances for wake flows to recover. The figure illustrates that, except for the second row of turbines, whose power output is accurately predicted by most of the models (excluding the Park model for the aforementioned reasons), all models systematically overestimate the power output further inside the wind farm. The Park and TurbOPark models exhibit a notably large overprediction deep into the wind farm. These results indicate that the performance of the models is affected by the wind farm configuration, and more specifically by the effective downstream distance between adjacent wind turbines. One possible reason for this dependence is the assumption of linear or quasi-linear expansion of the turbine wakes, which is likely to break down and overestimate the wake recovery at long downstream distances, as recently discussed by Vahidi and Porté-Agel [19]. That would explain why the prediction by some models like the one of Zong and Porté-Agel [17] is good for relatively short effective inter-turbine distances ($5D$ and $7D$ in the aligned cases), but it deteriorates with increasing distances ($10D$ and $14D$ in the staggered configurations). This observation can also be inferred from the predicted wind velocity fields plotted in Fig. 7.

3.3. Turbulence intensity prediction

3.3.1. Base model for a single turbine added turbulence intensity

Considering the importance of turbulence intensity on the wake growth rate estimation, in this section, we evaluate two common empirical relations for estimating the added streamwise turbulence intensity

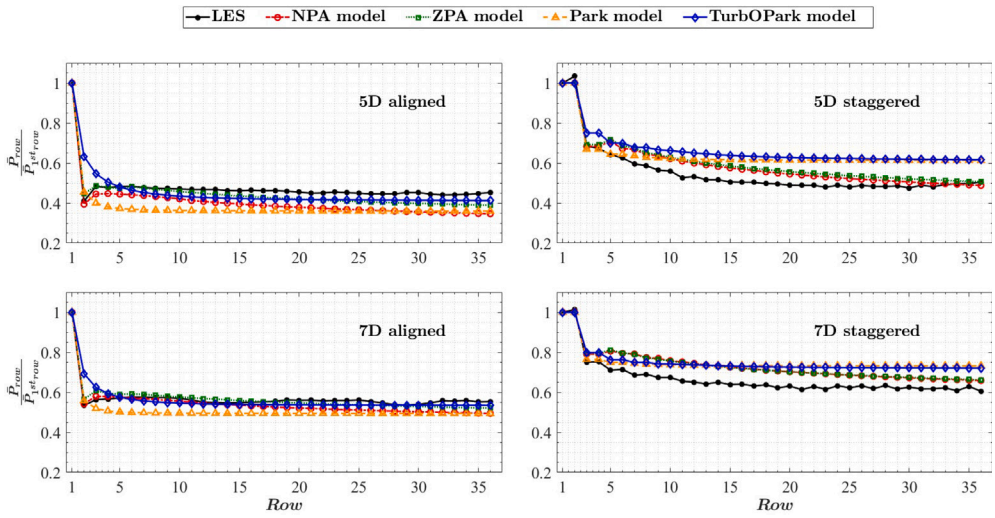

Fig. 9. Power output of different turbine rows inside the 36-row wind farms of different configurations normalized by the power output of the first row, as simulated by LES and predicted by all the considered analytical wake models: NPA model [16], ZPA model [17], Park model [12] and TurbOPark model [15].

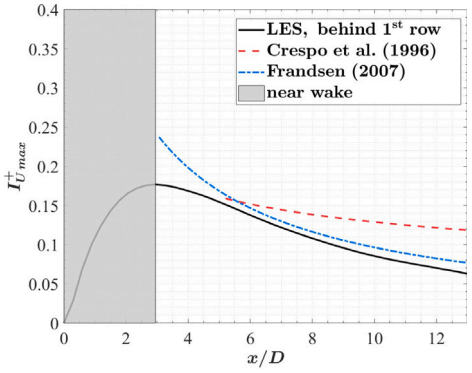

Fig. 10. Variation of the maximum streamwise added turbulence intensity ($I^+_{U\,max}$) behind the first row of the $7D$ staggered 9-row wind farm as simulated by LES, and predicted by Frandsen, and Crespo's models.

(I^+_U) by an individual turbine. The first empirical equation, proposed by Crespo and Hernández [23], estimates I^+_U as:

$$I_U^+ = 0.73 a^{0.8325} I_0^{-0.0325} \left(\frac{x}{D}\right)^{-0.32} \quad . \tag{13}$$

This equation is valid for $5 < \frac{x}{D} < 15$, with $0.07 < I_0 < 0.14$ and $0.1 < a < 0.4$, where a represents the induction factor.

The second empirical relation, developed by Frandsen [24] for the far wake region, is as follows:

$$I_U^+ = \frac{\sqrt{C_T}}{1.5\sqrt{C_T} + 0.3\sqrt{7}\left(\frac{x}{D}\right)} \quad . \tag{14}$$

In Fig. 10, the results of the considered added turbulence intensity models are compared to the LES output taken behind the first row of the staggered 9-row wind farm with a turbine spacing of $7D$. As shown by the LES results, the decay of I^+_U is more significant than predicted by Crespo's model. The comparison shows that Frandsen's model provides more accurate predictions of added turbulence intensity in the far wake compared to Crespo's model. Since we are interested in the far-wake region, Frandsen's relation is selected as the base model for estimating the added turbulence intensity by a given turbine in the new analytical model proposed in Section 3.6.

3.3.2. Turbulence intensity superposition method

In this section, we evaluate different methods to account for the effect of wake superposition on the turbulence intensity inside wind farms. As discussed by Li et al. [27], the existing superposition methods consider either the cumulative effect of the added turbulence from all upstream turbines or only the prevalent effect of the closest upstream turbine. Previous studies claimed that the turbulence intensity inside a wind farm can be approximated by the added turbulence from the closest adjacent upstream turbine [57]. This observation led to a non-cumulative approach, as implemented by Niayifar and Porté-Agel [16] and later also applied by Zong and Porté-Agel [17]:

$$I_{U_j}^+ = max\left(\frac{A_w}{A_0} I_{U_{kj}}^+\right) \quad , \tag{15}$$

where A_w is the cross-sectional area of the wake, A_0 the rotor swept area, $I^+_{U_{kj}}$ is the added streamwise turbulence intensity generated by an upstream turbine k at the location of a given turbine j inside a wind farm, and $I^+_{U_j}$ is the added streamwise turbulence intensity at the inlet of turbine j. The total turbulence intensity is calculated as:

$$I_{U_j} = \sqrt{I_0^2 + I_{U_j}^{+2}} \quad . \tag{16}$$

Another approach consists of applying the sum square method to superpose the added turbulence intensity, considering the effect of all the upstream turbines, instead of just the closest upstream one [27]. Specifically, the added turbulence intensity at the location of turbine j can be calculated as:

$$I_{U_j}^{+2} = \sum_k \left(\frac{A_w}{A_0} I_{U_{kj}}^+\right)^2 \quad . \tag{17}$$

The main difference between the method implemented here and the one of Li et al. [27] lies in their implementation of the 3D model developed by Li et al. [26] to estimate the individual turbine-added turbulence intensity. Here, we have opted for the simpler $1D$ model of Frandsen [24] since it provides reasonable predictions, as shown in Section 3.3.1.

3.3.3. Effect of wind speed used for normalization

The turbulence intensity is defined as the ratio of the standard deviation of wind speed fluctuations to the mean wind speed, and it is constituted of the undisturbed flow turbulence intensity and the added turbulence intensity generated by the turbine. As pointed out by Li et al. [27], the mean wind velocity used for the normalization can be either the undisturbed wind speed at the wind farm inlet or the local wind velocity inside the wind farm. In the context of a wind farm, using the

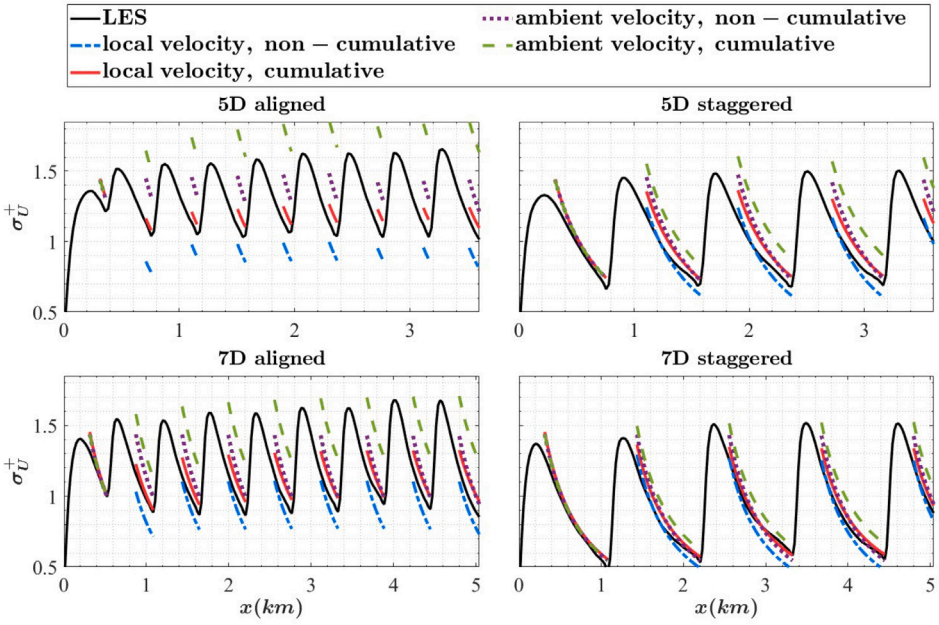

Fig. 11. Variation of the maximum added standard deviation of the streamwise wind velocity for the 9-row cases at the top-tip level of the turbines as simulated by LES and predicted by the various superposition methods considered.

local hub height wind speed for the normalization allows the analytical model to account for the local turbulence intensity, which is crucial for turbine load evaluation and provides a more representative estimation of wake losses as emphasized by Göçmen and Giebel [58].

Next, we evaluate different combinations of the two aforementioned superposition techniques (cumulative, Eq. (17) and non-cumulative, Eq. (15)) coupled with the two normalization approaches (using the local turbine inlet wind velocity and the farm inlet wind speed). Fig. 11 shows the standard deviation of the streamwise wind velocity component added to the undisturbed flow, obtained using the four resulting combinations of methods, as well as the corresponding values obtained from the LES simulations for the nine-row wind farms. The most accurate method, which closely matches the LES results across all wind farm configurations, is the one that uses the cumulatively added turbulence intensity equation (Eq. (17)) and utilizes the local wind velocity. The slight overestimation in the added turbulence intensity near the end of the six turbines column case observed by Li et al. [27] is not witnessed in the results shown in Fig. 11. On the contrary, the calculated standard deviation using the cumulative method with the local wind speed remains accurate even at the 9th row, the last row of the considered wind farm.

After analysing multiple combinations, the model presented in Section 3.6 computes the turbulence intensity within a wind farm using the most precise techniques identified. Specifically, we select the above-described Frandsen's model (Eq. (14)) as the base model for a single turbine added turbulence intensity $I_{U\,kj}^{+}$, the cumulative technique for the superposition of the added turbulence from all upstream turbines (Eq. (17)), and the local wind velocity U_j at a turbine inlet for the normalization. Consequently, the turbulence intensity is calculated as follows:

$$I_{U\,j} = \sqrt{I_0^2 \frac{U_\infty}{U_j} + \sum_k \left(\frac{A_w}{A_0} I_{U\,kj}^{+} \frac{U_k}{U_j} \right)^2} \quad . \tag{18}$$

3.4. Streamwise scaling for improved wake expansion modelling

As discussed in Section 3.2, the fact that most of the tested analytical wake models overestimate the wake recovery inside and downwind of the wind farms, particularly over relatively long effective streamwise inter-turbine distances, could be related to their assumption of linear or quasi-linear wake expansion. Vahidi and Porté-Agel [19] showed that, for a stand-alone wind turbine wake, this assumption does not hold at relatively long downstream distances. In a follow-up study, they proposed a simple new streamwise scaling model based on the observation that the wake width of an individual turbine, normalized by the rotor diameter, collapses into a single curve if plotted against the downstream distance, normalized by the near-wake length [20]. The model computes the normalized maximum velocity deficit ΔU_{max} based on its universal relation with respect to the downstream distance normalized by the near-wake length, as follows:

$$\frac{\Delta U_{max}}{U_\infty \left(1 - \sqrt{1 - C_T}\right)} = 1.75 \left(\frac{x}{x_{NW}} + 0.5 \right)^{-1.37} \quad . \tag{19}$$

After computing ΔU_{max}, one can calculate the wake width σ based on the following equation derived from momentum conservation [11]:

$$\frac{\Delta U_{max}}{U_\infty} = 1 - \sqrt{1 - \frac{C_T}{8(\sigma/D)^2}} \quad . \tag{20}$$

Fig. 12(a) shows a comparison of the wake width normalized by the rotor diameter computed from the streamwise scaling model of Vahidi and Porté-Agel [20], the wake growth rate relations proposed by Niayifar and Porté-Agel [16] and Shapiro et al. [46], and that obtained from the LES data, as a function of the streamwise distance normalized by the near-wake length, at the first row of a $7D$ staggered case, where the streamwise distance between turbines is the largest. From LES, the σ values are obtained by fitting the wind velocity deficit profiles downwind of the turbine using a Gaussian function. We define the near-wake length as the distance between the wind turbine and the downstream location where the linear correlation coefficient of the Gaussian fit exceeds the commonly assumed value of 0.99 [19,20,59,60]. The results in Fig. 12(a) confirm the findings of Vahidi and Porté-Agel [19], who showed that σ does not vary linearly with the downstream distance. Both the linear function of Niayifar and Porté-Agel [16] and the quasi-linear function of Shapiro et al. [46] overestimate the wake width beyond a normalized downwind distance of $8D$.

In Fig. 12(b) the normalized maximum wind velocity deficit variation obtained from the four different methods is represented with respect to the streamwise distance normalized by the near-wake length.

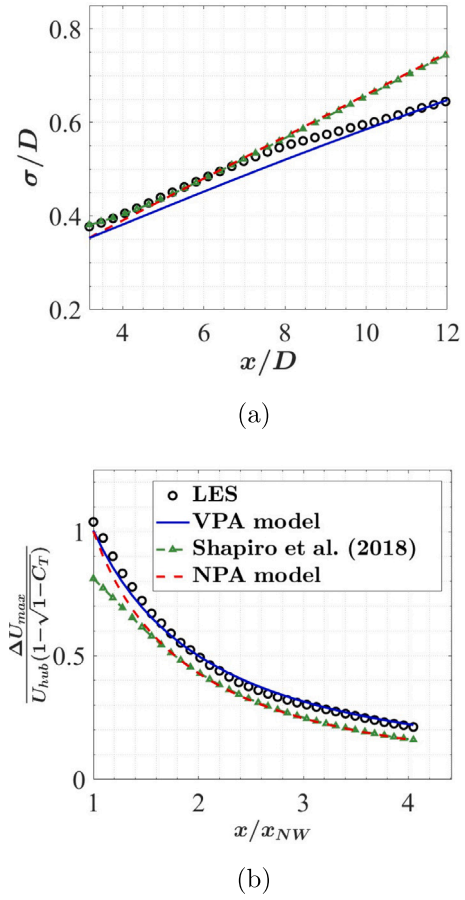

Fig. 12. (a) The wake width as a function of streamwise distance normalized by the rotor diameter. (b) The normalized maximum wake velocity deficit as a function of the streamwise distance normalized by the near-wake length. Both plots are taken downstream of a turbine at the first row of the 9-row 7D staggered case. The black circles indicate the LES results and the solid blue line is the solution obtained from the streamwise scaling model of VPA [20]. The prediction by the wake growth rate relation of NPA model [16] is shown in a dashed red line and of Shapiro et al. [46] in green.

The results are accurately predicted by the streamwise scaling model. On the other hand, using the σ values obtained from the relation of Bastankhah and Porté-Agel [22], in which the wake growth rate equation of Niayifar and Porté-Agel [16] is implemented, and the relation of Shapiro et al. [46] in the Gaussian model leads to an underestimation of the actual maximum wind velocity deficit, which is consistent with the previously identified overestimation of the wake recovery rate. Specifically, the fact that the largest errors were detected in staggered wind farms could be attributed to the relatively large effective streamwise distance between wind turbines (exceeding $8D$) in those cases. Based on the aforementioned observations, the streamwise scaling method offers the most accurate representation of turbine wake expansion, especially at far downwind distances and high turbulence intensity levels that are commonly encountered inside wind farms. As a result, the streamwise scaling method is implemented and extended to account for the interaction of multiple turbine wakes within and downstream of wind farms in the analytical wake modelling framework proposed in Section 3.6.

3.5. Near-wake length model

The near-wake length is a key parameter in several analytical wake models. Here we evaluate the performance of three available near-wake length parameterizations. The first tested model is the one proposed by Vermeulen [21]:

$$\left.\begin{aligned} x_{NW} &= \frac{D}{2}\sqrt{\frac{m+1}{2}}\frac{\left(1-\sqrt{0.134+0.124m}\right)\sqrt{0.214+0.144m}}{\left(1-\sqrt{0.214+0.144m}\right)\sqrt{0.134+0.124m}}(k^*)^{-1} \quad , \\ k^* &= \sqrt{(k^*)_\alpha^2+(k^*)_s^2+(k^*)_\lambda^2} \quad , \\ (k^*)_\alpha &= 2.5I_0+0.005 \quad , \\ (k^*)_s &= \frac{(1-m)\sqrt{1.49+m}}{9.76(1+m)} \quad , \\ (k^*)_\lambda &= 0.012N_b\Lambda \quad . \end{aligned}\right\} \tag{21}$$

In this model, the wake growth rate (k^*) is decomposed into the contribution of three turbulence components: ambient turbulence (α), shear-generated turbulence (s), and turbine-generated turbulence (λ). The parameter m is set equal to $m = \frac{1}{\sqrt{1-C_T}}$, N_b is the number of blades and Λ is the tip speed ratio.

The second model is a semi-empirical relationship derived by Bastankhah and Porté-Agel [22], which is based on an analogy with round co-flowing jets:

$$x_{NW} = \frac{D(1+\sqrt{1-C_T})}{\sqrt{2}\left[4\alpha I_U + 2\beta\left(1-\sqrt{1-C_T}\right)\right]} \quad , \tag{22}$$

where $\beta = 0.154$ is an analytical constant and $\alpha = 2.32$ is an empirical parameter.

The third model considered here is the model of Vahidi and Porté-Agel [19], which is based on the analogy between wind turbine wake expansion and scalar diffusion from a disk source. For the case of near-neutral atmospheric conditions, which are applicable to this study, it can be written as follows:

$$x_{NW} = x_0 + \sigma_e \frac{D\left(1+\sqrt{1-C_T}\right)}{2\left[\sqrt{Sc_t}\left(0.63I_U\right)+S'\left(1-\sqrt{1-C_T}\right)\right]} \quad , \tag{23}$$

where standard values are adopted for the turbulence Schmidt number $Sc_t = 0.5$, the mixing layer characteristic length spreading rate $S' = 0.043$, and the threshold for the onset of the far-wake $\sigma_e = 0.18$. In the expansion region of length (x_0), pressure builds up to reach the ambient pressure with negligible shear layer growth compared to the rotor diameter [61]. It is assumed that this region spans over one rotor diameter based on experimental findings [62] and 1D momentum theory [63] for a turbine operating at its optimal tip speed ratio.

It is worth noting that the two latter models require the turbulence intensity at the turbine inlet (I_U) as an input. As discussed in Section 3.3, the locally calculated turbulence intensity is utilized. On the other hand, the model by Vermeulen [21] considers each source of turbulence separately. Instead of relying on the local turbulence intensity as in the other two models, this allows the use of the undisturbed flow turbulence intensity level (I_0) for the ambient turbulence component $\left[(k^*)_\alpha\right]$ across the wind farm, normalized by the local wind speed at the turbine inlet.

The findings from the three tested near-wake length models are shown in Fig. 13 and compared with the corresponding LES results. It is observed that the near-wake length of the turbines at the first row is accurately predicted by the model developed by Vahidi and Porté-Agel [19]. Inside a wind farm, the near-wake length decreases sharply in waked conditions. Yet, none of the considered models accurately predict the near-wake length inside the wind farm. Based on our results, and considering that the model of Vahidi and Porté-Agel [19] systematically overestimates the near-wake length in waked conditions by about $0.5D$, a modified version of this model is proposed that employs an expansion region of $0.5D$ (instead of $1D$) in waked wind turbines within the wind farm. As shown in Fig. 13 when comparing the

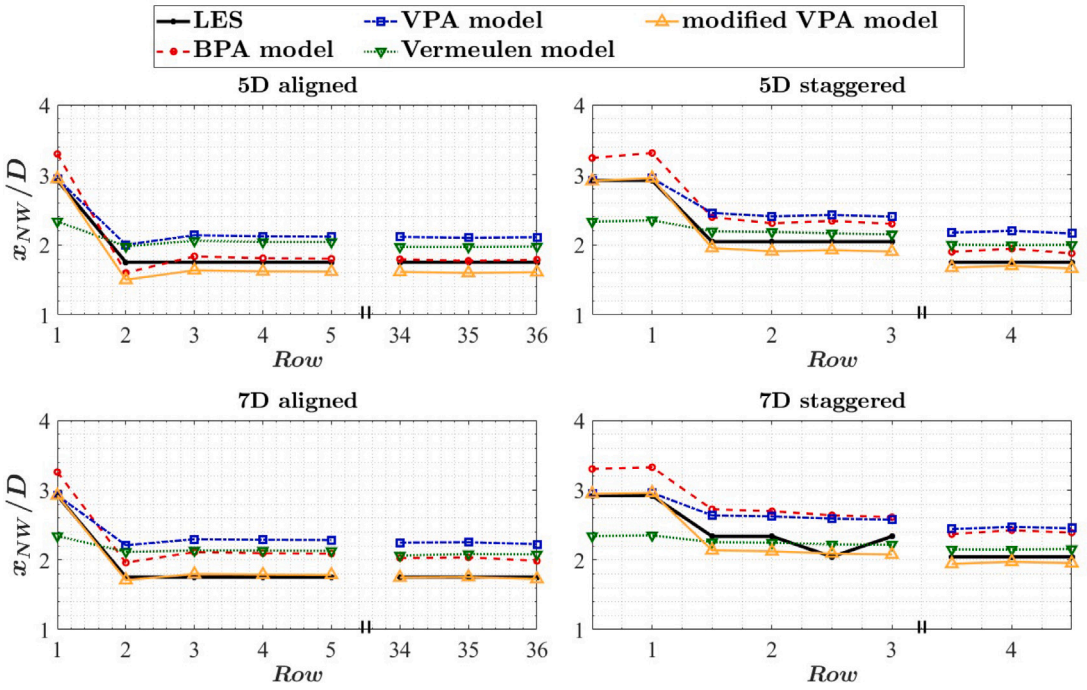

Fig. 13. Near-wake length variation inside all the 36-row wind farms: Comparison of LES results with predictions by the models of Vermeulen [21], BPA [22], and VPA [19] in both its original and modified version.

original near-wake model to the modified one, the new implementation with the shorter expansion region yields a better prediction for the largest 36-row wind farm. Based on these results, it is recommended to use two distinct expansion region lengths: $x_0 = 1D$ for the turbines at the first row in unwaked conditions and $x_0 = 0.5D$ for the waked turbines inside the wind farm. Additional research is necessary to gain a better understanding of the physical causes behind the change in the expansion region inside wind farms.

3.6. Proposed analytical framework for wind farm flow predictions

Based on the results presented in the previous sections, here we propose an analytical framework for wind farm flow modelling. It is based on the extension of the model of Vahidi and Porté-Agel [20] for single turbines to a wind farm. The method for wake superposition considered is the momentum conserving superposition technique developed by Zong and Porté-Agel [17]. The methods to calculate key components of the model, including the turbulence intensity and its superposition inside the wind farm, the near-wake length, and the wake width, are summarized below:

- The normalized maximum wind velocity deficit in the turbine wake is calculated using the streamwise scaling method introduced by Vahidi and Porté-Agel [20] represented by the following equation resulting from rearranging Eq. (19):

$$\frac{\Delta U_{max}}{U_\infty} = 1.75\left(\frac{x}{x_{NW}} + 0.5\right)^{-1.37} \cdot \left(1 - \sqrt{1 - C_T}\right)$$

- The turbine wake width (σ) (standard deviation of the Gaussian velocity deficit) is computed from the normalized maximum velocity deficit using the model of Bastankhah and Porté-Agel [11] to guarantee the conservation of momentum. Specifically, rearranging Eq. (20) yields:

$$\sigma/D = \sqrt{\frac{C_T}{8\left[1 - \left(1 - \frac{\Delta U_{max}}{U_\infty}\right)^2\right]}}$$

- The near-wake length is estimated using the model proposed by Vahidi and Porté-Agel [19] with an expansion region length of $x_0 = 1D$ for turbines in unwaked conditions and $x_0 = 0.5D$ for waked turbines inside the wind farm. It is given by Eq. (23):

$$x_{NW} = x_0 + \sigma_e \frac{D\left(1 + \sqrt{1 - C_T}\right)}{2\left[\sqrt{Sc_t}\left(0.63 I_U\right) + S'\left(1 - \sqrt{1 - C_T}\right)\right]}$$

- The turbulence intensity superposition method uses the local wind velocity at the inlet of each turbine and incorporates the cumulative effect of added turbulence from all upstream turbines. The selected superposition and normalization techniques are represented by Eq. (18):

$$I_{U\,j} = \sqrt{I_0^2 \frac{U_\infty}{U_j} + \sum_k \left(\frac{A_w}{A_0} I^+_{U\,kj} \frac{U_k}{U_j}\right)^2}$$

- The added turbulence intensity behind each turbine is determined using the model developed by Frandsen [24] (Eq.: (14)):

$$I^+_{U\,kj} = \frac{\sqrt{C_T}}{1.5\sqrt{C_T} + 0.3\sqrt{7}\left(\frac{x}{D}\right)}$$

The proposed analytical framework is tested for all the considered wind farm sizes and configurations in this study. Fig. 14 shows the power output from LES and the power computed by implementing the proposed model, as well as the model of Zong and Porté-Agel [17]. Only the largest wind farm results are presented here since in Section 3.1 it is shown that the power output variation inside a wind farm remains the same for all the considered sizes. Overall, the proposed model yields more accurate power predictions, and it is able to rectify the systematic overestimation obtained with all the previously tested analytical models shown in Fig. 9.

Consistent with the improved power prediction, the new model yields also enhanced predictions of the mean wind speed. Fig. 15 shows the streamwise variation of the rotor-averaged wind speed at hub height inside and in the wake region of the wind farms with 36 rows and all considered configurations. Comparing the output from the

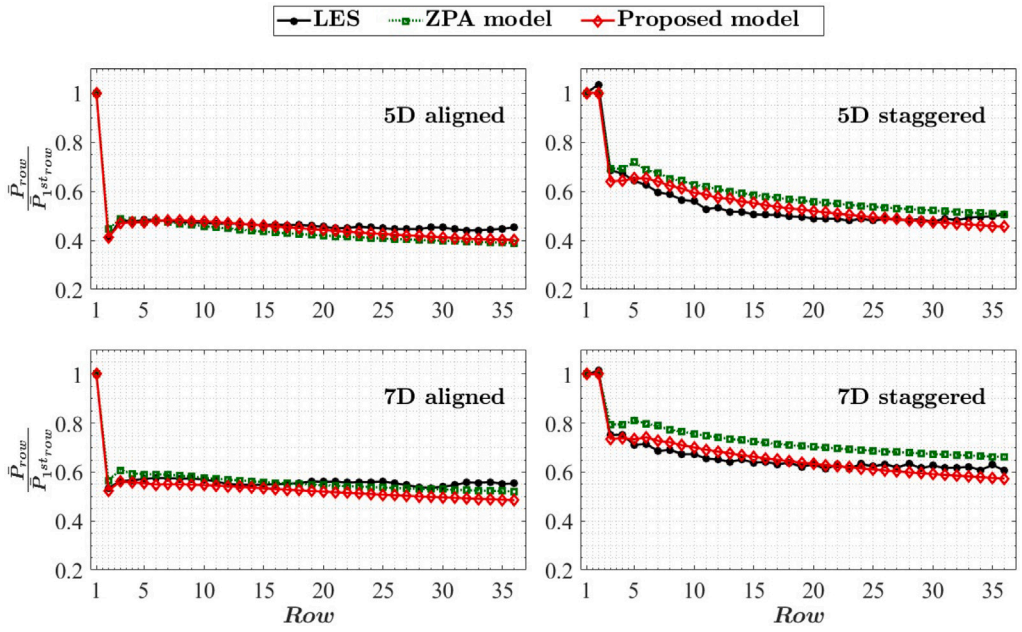

Fig. 14. Normalized row power output of the 36 rows wind farms of different configurations, as simulated by LES and predicted by the proposed model and ZPA model [17].

implemented models to the LES data, it is concluded that the proposed framework yields the most accurate wind velocity estimation inside the wind farm as well as in the wind farm wake, notably near the exit of the wind farm where all the previously evaluated models overestimated the wind velocity. The same improvement is observed with all the tested configurations, showing that the proposed model is robust and accurate for all wind farm layouts and densities. In Fig. 16, we present the streamwise variation of the rotor-averaged wind speed at hub height inside and in the wake region of the $7D$ staggered wind farms for all considered sizes. Similarly, a comparison of the outputs from the analytical models against LES data reveals that the proposed framework consistently provides the most accurate wind velocity estimations both in the inter-turbine regions and within the wind farm wake. Hence, the proposed model can also yield accurate wind speed predictions inside and downwind of the wind farm irrespective of its size. The improved wake prediction by the proposed model can also be observed in Fig. 17. It depicts contour plots of the time-averaged wind speed at hub height within and downstream of the 9-row wind farms from LES, the analytical wake models of Niayifar and Porté-Agel [16] and Zong and Porté-Agel [17], and the proposed model. It is shown that the proposed model improves the wake prediction inside and downstream of the wind farm. Overall, the extent of the turbine wakes and their spanwise interactions inside the wind farm and in the wake region are better predicted by the new model. These enhancements can be attributed to the new approach for calculating the wake width using the streamwise scaling technique and the modified method for accounting for the superposition of turbulence intensity inside the wind farm. These features of the new model allow it to mitigate the overestimation of the wake growth rate exhibited by the tested analytical wake models.

4. Summary

This study presents a comprehensive evaluation of available analytical wake models and proposes an enhanced modelling framework for flow prediction inside and downstream of wind farms using LES data of sixteen different wind farms with varying sizes and layouts within a CNBL. The LES results reveal a clear effect of wind farm size, layout and density on the flow in the wind farm exit and wind farm wake regions. For the typical size range of existing and planned wind farms, and for a particular layout, increasing the wind farm size leads to a reduction in the spanwise-averaged mean wind speed at any given distance relative to the wind farm exit. For the largest considered wind farms, the flow and power output deep inside the wind farm show less variability with farm size and become closer to those found in infinite wind farms, albeit not reaching them. As expected, increasing wind farm density leads to a decrease in wind speed, thus power output per turbine, deep inside the wind farms and in their wakes. As for the effect of changing the layout, fully aligned configurations, characterized by relatively shorter streamwise and longer spanwise effective inter-turbine distances, produce larger spanwise flow heterogeneity than their staggered counterparts. This explains the fact that they lead to larger power losses while yielding larger spanwise-averaged wind speed in the wind farm exit and wake region.

The following analytical models are evaluated against the LES data: the Park model, the TurbOPark model, the framework of Niayifar and Porté-Agel [16], and the momentum conserving framework of Zong and Porté-Agel [17]. All the tested models tend to over-predict the wake recovery behind the turbines inside and downstream of the wind farms for all the considered sizes and layouts. As a result, the power output over the wind farm rows is not well predicted. Our results show that an important factor contributing to the overestimation of the wake recovery by some of the analytical models is the assumption of a linear or quasi-linear wake expansion rate. Analysis of the LES data reveals that this linear relationship is not valid at relatively long distances downwind of wind turbines, which is consistent with the findings of Vahidi and Porté-Agel [19] for a single turbine.

To address the aforementioned wake recovery overestimation, we propose a new analytical framework extending the recently developed model by Vahidi and Porté-Agel [20] for stand-alone wind turbines, which does not rely on the linear wake expansion assumption, to

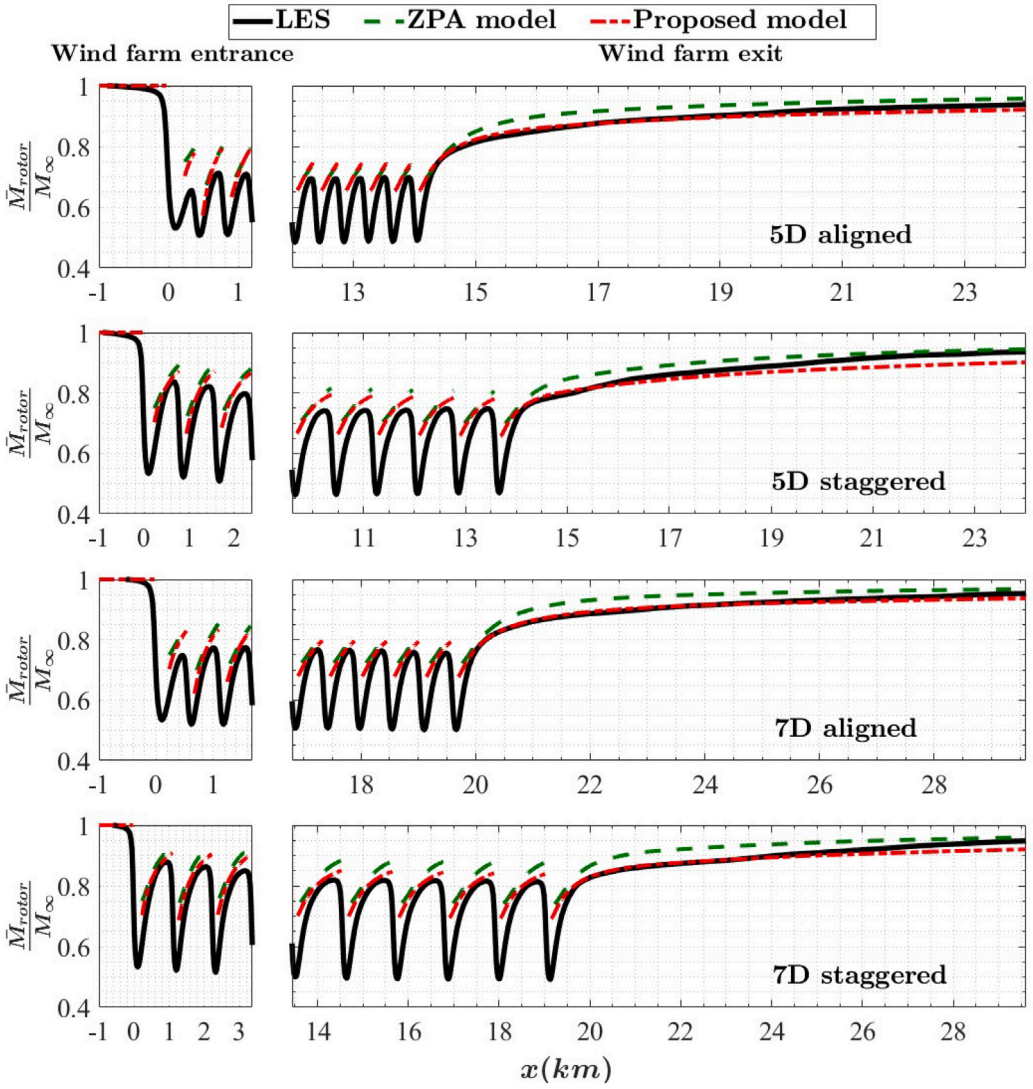

Fig. 15. Rotor-averaged wind velocity variation near the entrance and exit of the 36 rows wind farms of different configurations and their wake region, as simulated by LES and predicted by the proposed model and the ZPA model [17].

the flow prediction inside and downstream of wind farms. The proposed framework depends on estimating the near-wake length and turbulence intensity within a wind farm, crucial for prescribing the non-linear growth rate. In this context, various methods for calculating the near-wake length, turbulence intensity and its superposition are assessed against the LES data. For the near-wake length, the method developed by Vahidi and Porté-Agel [19] is found to yield the most accurate predictions. For the added turbulence intensity by a single turbine, the relation of Frandsen [24] is shown to be the most accurate. Furthermore, the study establishes the necessity of adopting a cumulative superposition methodology to account for the combined effect of the added turbulence intensity from all the wind turbines upstream. Additionally, it is recommended to normalize the standard deviation of wind velocity with the local wind speed within the wind farm instead of using the undisturbed flow velocity at the wind farm inlet.

Compared with LES, the proposed analytical modelling framework yields improved power estimates and wind speed predictions both inside and downstream of wind farms with respect to the other tested analytical wake models. The improved framework also exhibits robustness by achieving the same level of accuracy in the wake prediction for all considered cases regardless of the wind farm size, density and configuration. In future work, we aim to study the effects of surface-layer thermal stratification on wind farm wakes and assess the ability of different analytical wake models (including the newly developed framework) to predict those impacts.

CRediT authorship contribution statement

Marwa Souaiby: Conceptualization, Data curation, Formal analysis, Investigation, Methodology, Visualization, Writing – original draft. **Fernando Porté-Agel:** Conceptualization, Funding acquisition, Methodology, Resources, Supervision, Writing – review & editing.

Declaration of competing interest

The authors declare that they have no known competing financial interests or personal relationships that could have appeared to influence the work reported in this paper.

Acknowledgements

This work is part of the Train2Wind project that received funding from the European Union's Horizon 2020 research and innovation program under the Marie Sklodowska-Curie grant agreement No. 861291.

Computing resources were provided by the Swiss National Supercomputing Centre (CSCS) and by EPFL through its Scientific IT and Application Support Center (SCITAS).

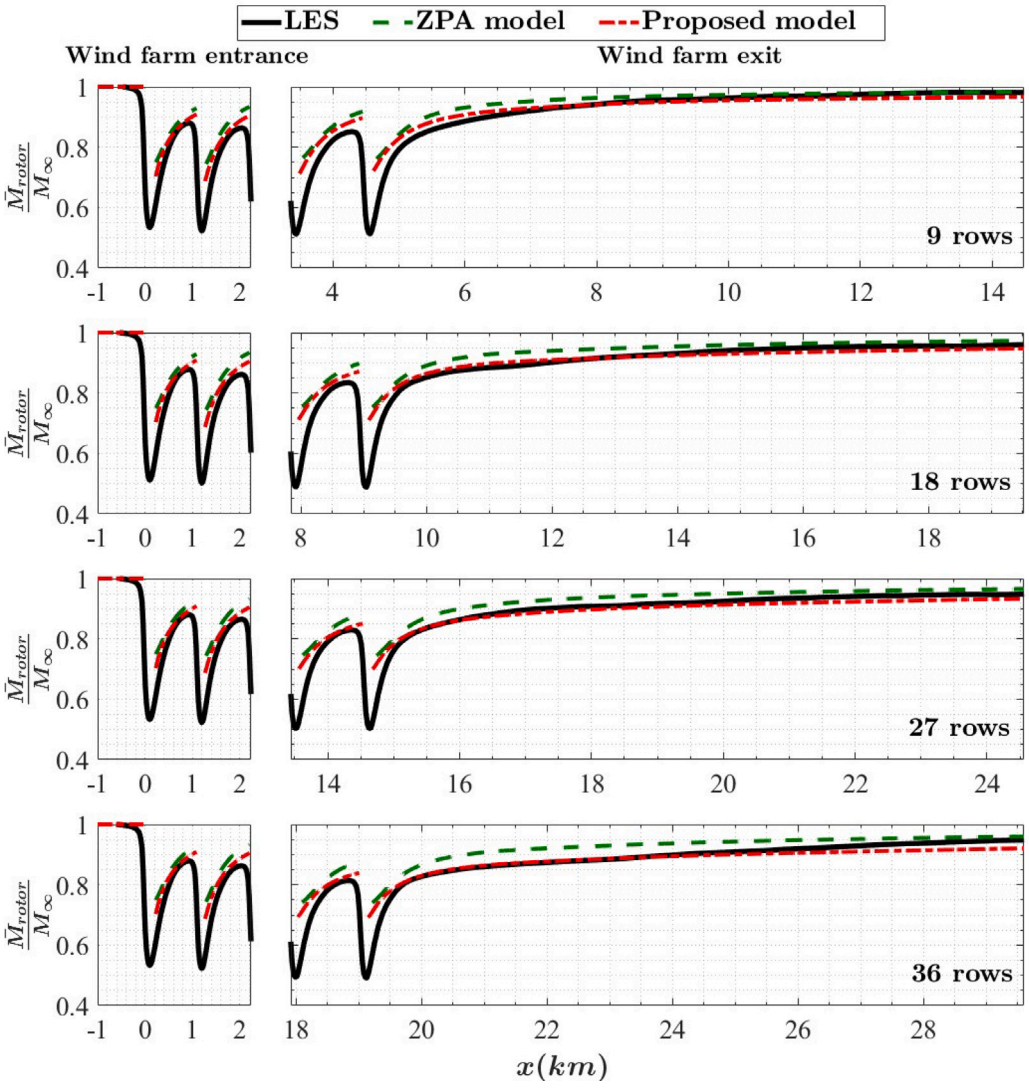

Fig. 16. Rotor-averaged wind velocity variation near the entrance and exit of the 7D staggered wind farms of different sizes and their wake region, as simulated by LES and predicted by the proposed model and the ZPA model [17].

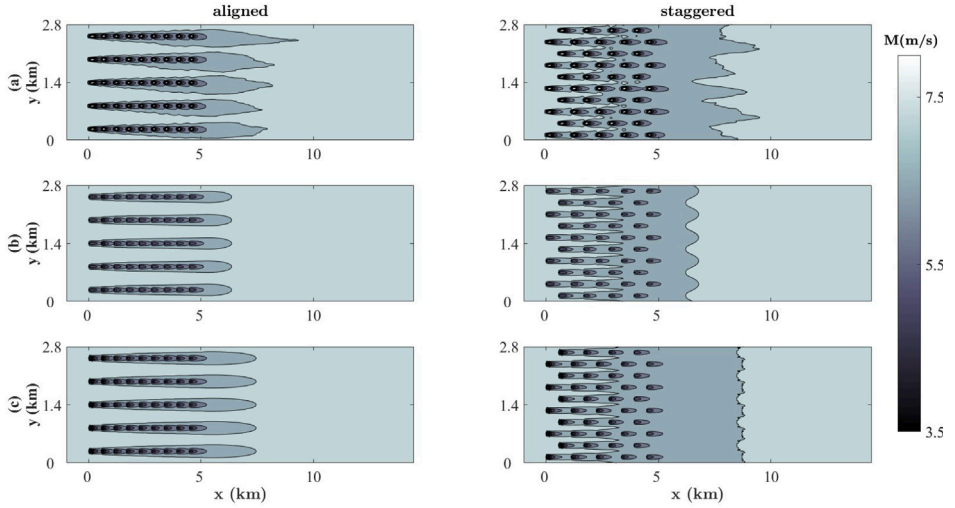

Fig. 17. Contours of the time-averaged mean wind velocity magnitude at a horizontal plane at hub height in the 9-row wind farm cases, aligned and staggered, with 7D turbine spacing from (a) LES, (b) the model of Zong and Porté-Agel [17], and (d) the proposed model implementing the momentum conserving superposition method.

References

[1] G. Costanzo, G. Brindley, P. Cole, Wind energy in Europe: 2022 statistics and the outlook for 2023–2027, WindEurope (2023).
[2] European Commission, The European climate law, Dir. Gener. Commun. (2021).
[3] R.J. Barthelmie, S.C. Pryor, S.T. Frandsen, K.S. Hansen, J.G. Schepers, K. Rados, W. Schlez, A. Neubert, L.E. Jensen, S. Neckelmann, Quantifying the impact of wind turbine wakes on power output at offshore wind farms, J. Atmos. Ocean. Technol. 27 (8) (2010) 1302–1317.
[4] F. Porté-Agel, Y.T. Wu, C.H. Chen, A numerical study of the effects ofwind direction on turbine wakes and power losses in a largewind farm, Energies 6 (2013) 5297–5313.
[5] R.J. Stevens, D.F. Gayme, C. Meneveau, Large eddy simulation studies of the effects of alignment and wind farm length, J. Renew. Sustain. Energy 6 (2014).
[6] J. Schneemann, A. Rott, M. Dörenkämper, G. Steinfeld, M. Kühn, Cluster wakes impact on a far-distant offshore wind farm's power, Wind Energy Sci. 5 (2020) 29–49.
[7] S.P. Breton, J. Sumner, J.N. Sørensen, K.S. Hansen, S. Sarmast, S. Ivanell, A survey of modelling methods for high-fidelity wind farm simulations using large eddy simulation, Phil. Trans. R. Soc. A 375 (2017).
[8] F. Porté-Agel, M. Bastankhah, S. Shamsoddin, Wind-turbine and wind-farm flows: A review, Bound.-Lay. Meteorol. 174 (2020) 1–59.
[9] N.O. Jensen, A Note on Wind Generator Interaction, Risø-M-2411 Risø National Laboratory Roskilde, 1983, pp. 1–16.
[10] S. Frandsen, R. Barthelmie, S. Pryor, O. Rathmann, S. Larsen, Analytical modelling of wind speed deficit in large offshore wind farms, Control 9 (2006) 39–53.
[11] M. Bastankhah, F. Porté-Agel, A new analytical model for wind-turbine wakes, Renew. Energy 70 (2014) 116–123.
[12] I. Katic, J. Hojstrup, N. Jensen, A simple model for cluster efficiency, in: W. Palz, E. Sesto (Eds.), EWEC'86. Proceedings, Raguzzi, A., Rome, 1986, pp. 407–410.
[13] R. Stevens, D. Gayme, C. Meneveau, Generalized coupled wake boundary layer model: applications and comparisons with field and LES data for two wind farms, Wind Energy 19 (2016).
[14] M. Calaf, C. Meneveau, J. Meyers, Large eddy simulation study of fully developed wind-turbine array boundary layers, Phys. Fluids 22 (2010) 015110.
[15] N.G. Nygaard, S.T. Steen, L. Poulsen, J.G. Pedersen, Modelling cluster wakes and wind farm blockage, J. Phys. Conf. Ser. 1618 (2020).
[16] A. Niayifar, F. Porté-Agel, Analytical modeling of wind farms: A new approach for power prediction, Energies 9 (2016) 741.
[17] H. Zong, F. Porté-Agel, A momentum-conserving wake superposition method for wind farm power prediction, J. Fluid Mech. 889 (2020) A8.
[18] A. Stieren, R.J.A.M. Stevens, Evaluating wind farm wakes in large eddy simulations and engineering models, J. Phys. Conf. Ser. 1934 (2021) 012018.
[19] D. Vahidi, F. Porté-Agel, A physics-based model for wind turbine wake expansion in the atmospheric boundary layer, J. Fluid Mech. 943 (2022) 1–28.
[20] D. Vahidi, F. Porté-Agel, A new streamwise scaling for wind turbine wake modeling in the atmospheric boundary layer, Energies 15 (24) (2022) 9477.
[21] P. Vermeulen, An experimental analysis of wind turbine wakes, in: 3rd International Symposium on Wind Energy Systems, 1980, pp. 431–450.
[22] M. Bastankhah, F. Porté-Agel, Experimental and theoretical study of wind turbine wakes in yawed conditions, J. Fluid Mech. 806 (2016) 506–541.
[23] A. Crespo, J. Hernández, Turbulence characteristics in wind-turbine wakes, J. Wind Eng. Ind. Aerodyn. 61 (1996) 71–85.
[24] S. Frandsen, Turbulence and turbulence- generated structural loading in wind turbine clusters, 2007.
[25] T. Ishihara, G.-W. Qian, A new Gaussian-based analytical wake model for wind turbines considering ambient turbulence intensities and thrust coefficient effects, J. Wind Eng. Ind. Aerodyn. 177 (2018) 275–292.
[26] L. Li, Z. Huang, M. Ge, Q. Zhang, A novel three-dimensional analytical model of the added streamwise turbulence intensity for wind-turbine wakes, Energy 238 (2022).
[27] L. Li, B. Wang, M. Ge, Z. Huang, X. Li, Y. Liu, A novel superposition method for streamwise turbulence intensity of wind-turbine wakes, Energy 276 (February) (2023) 127491.
[28] F. Porté-Agel, C. Meneveau, M. Parlange, A scale-dependent dynamic model for large-eddy simulation: Application to a neutral atmospheric boundary layer, J. Fluid Mech. 415 (2000) 261–284.
[29] R. Stoll, F. Porté-Agel, Dynamic subgrid-scale models for momentum and scalar fluxes in large-eddy simulations of neutrally stratified atmospheric boundary layers over heterogeneous terrain, Water Resour. Res. 42 (2006) 1–18.
[30] Y. Wu, F. Porté-Agel, Large-eddy simulation of wind-turbine wakes: Evaluation of turbine parametrisations, Bound.-Lay. Meteorol. 138 (2011) 345–366.
[31] F. Porté-Agel, Y. Wu, H. Lu, R. Conzemius, Large-eddy simulation of atmospheric boundary layer flow through wind turbines and wind farms, J. Wind Eng. Ind. Aerodyn. 99 (2011) 154–168.
[32] Y. Wu, Large-Eddy Simulation of Turbulent Boundary Layer Flow through Wind Turbines and Wind Farms (Ph.D. Thesis), 5788, EPFL, 2013.
[33] Y. Wu, F. Porté-Agel, Modeling turbine wakes and power losses within a wind farm using LES: An application to the Horns Rev offshore wind farm, Renew. Energy 75 (2015) 945–955.
[34] J.D. Albertson, M.B. Parlange, Surface length scales and shear stress: Implications for land-atmosphere interaction over complex terrain, Water Resour. Res. 35 (1999) 2121–2132.
[35] M. Abkar, F. Porté-Agel, The effect of free-atmosphere stratification on boundary-layer flow and power output from very large wind farms, Energies 6 (2013) 2338–2361.
[36] H. Lu, F. Porté-Agel, Large-eddy simulation of a very large wind farm in a stable atmospheric boundary layer, Phys. Fluids 23 (2011).
[37] R. Stoll, F. Porté-Agel, Surface heterogeneity effects on regional-scale fluxes in stable boundary layers: Surface temperature transitions, J. Atmos. Sci. 66 (2009) 412–431.
[38] A. Monin, A. Obukhov, Basic laws of turbulent mixing in the ground layer of the atmosphere, Trans. Geophys. Inst. Akad. Nauk 24 (1954) 163–187.
[39] C.-H. Moeng, A large eddy-simulation model for the study of planetary boundary-layer turbulence, J. Atmos. Sci. 41 (1984) 2052–2062.
[40] M. Abkar, F. Porté-Agel, A new boundary condition for large-eddy simulation of boundary-layer flow over surface roughness transitions, J. Turbul. 13 (2012) N23.
[41] A. Sescu, C. Meneveau, A control algorithm for statistically stationary large-eddy simulations of thermally stratified boundary layers, Q. J. R. Meteorol. Soc. 140 (2014) 2017–2022.
[42] M. Abkar, A. Sharifi, F. Porté-Agel, Wake flow in a wind farm during a diurnal cycle, J. Turbul. 17 (2016) 420–441.
[43] K. Wu, F. Porté-Agel, Flow adjustment inside and around large finite-size wind farms, Energies 10 (2017) 4–9.
[44] Y. Wu, F. Porté-Agel, Atmospheric turbulence effects on wind-turbine wakes: An LES study, Energies 5 (2012) 5340–5362.
[45] S. Frandsen, On the wind speed reduction in the center of large clusters of wind turbines, J. Wind Eng. Ind. Aerodyn. 39 (1992) 251–265.
[46] C.R. Shapiro, D.F. Gayme, C. Meneveau, Modelling yawed wind turbine wakes: A lifting line approach, J. Fluid Mech. 841 (2018) R11–R112.
[47] M.B. Christiansen, C.B. Hasager, Wake effects of large offshore wind farms identified from satellite SAR, Remote Sens. Environ. 98 (2005) 251–268.
[48] R.J. Barthelmie, S.T. Frandsen, M.N. Nielsen, S.C. Pryor, P.-E. Rethore, H.E. Jørgensen, Modelling and measurements of power losses and turbulence intensity in wind turbine wakes at Middelgrunden offshore wind farm, Wind Energy 10 (6) (2007) 517–528.
[49] R. Barthelmie, L. Jensen, Evaluation of wind farm efficiency and wind turbine wakes at the Nysted offshore wind farm, Wind Energy 13 (2010) 573–586.
[50] K. Hansen, R. Barthelmie, L. Jensen, A. Sommer, The impact of turbulence intensity and atmospheric stability on power deficits due to wind turbine wakes at Horns Rev wind farm, Wind Energy 15 (2012) 183–196.
[51] N.G. Nygaard, Wakes in very large wind farms and the effect of neighbouring wind farms, J. Phys. Conf. Ser. 524 (2014).
[52] C.D. Markfort, W. Zhang, F. Porté-Agel, Turbulent flow and scalar transport through and over aligned and staggered wind farms, J. Turbul. 13 (2012) 1–36.
[53] Y.T. Wu, F. Porté-Agel, Simulation of turbulent flow inside and above wind farms: Model validation and layout effects, Bound.-Lay. Meteorol. 146 (2013) 181–205.
[54] K.L. Wu, F. Porté-Agel, Flow adjustment inside and around large finite-size wind farms, Energies 10 (2017) 4–9.
[55] R. Barthelmie, K. Hansen, S. Frandsen, O. Rathmann, J. Schepers, W. Schlez, J. Phillips, K. Rados, A. Zervos, E. Politis, P. Chaviaropoulos, Modelling and measuring flow and wind turbine wakes in large wind farms offshore, Wind Energy 12 (2009) 431–444.
[56] R.J. Stevens, Dependence of optimal wind turbine spacing on wind farm length, Wind Energy 19 (2016) 651–663.
[57] S. Frandsen, M. Thøgersen, Integrated fatigue loading for wind turbines in wind farms by combining ambient turbulence and wakes, Wind Eng. 23 (1999) 327–339.
[58] T. Göçmen, G. Giebel, Estimation of turbulence intensity using rotor effective wind speed in lillgrund and Horns Rev-i offshore wind farms, Renew. Energy 99 (2016) 524–532.
[59] J.N. Sørensen, R.F. Mikkelsen, D.S. Henningson, S. Ivanell, S. Sarmast, S.J. Andersen, Simulation of wind turbine wakes using the actuator line technique, Phil. Trans. R. Soc. A 373 (2035) (2015) 20140071.
[60] F. Carbajo Fuertes, C.D. Markfort, F. Porté-Agel, Wind turbine wake characterization with nacelle-mounted wind lidars for analytical wake model validation, Remote Sens. 10 (5) (2018).
[61] A. Crespo, J. Hernández, S. Frandsen, Survey of modelling methods for wind turbine wakes and wind farms, Wind Energy 2 (1) (1999) 1–24, http://dx.doi.org/10.1002/(sici)1099-1824(199901/03)2:1<1::aid-we16>3.3.co;2-z.
[62] P.-Å. Krogstad, M.S. Adaramola, Performance and near wake measurements of a model horizontal axis wind turbine, Wind Energy 15 (5) (2012) 743–756, http://dx.doi.org/10.1002/we.502.
[63] M. Hansen, Aerodynamics of Wind Turbines, third ed., Routledge, 2015, http://dx.doi.org/10.4324/9781315769981.